



Theses and Dissertations

2015-06-01

A Feasibility Study of Photometric Reverberation Mapping with Meter-Class Telescopes

Carla June Carroll
Brigham Young University - Provo

Follow this and additional works at: <https://scholarsarchive.byu.edu/etd>



Part of the [Astrophysics and Astronomy Commons](#), and the [Physics Commons](#)

BYU ScholarsArchive Citation

Carroll, Carla June, "A Feasibility Study of Photometric Reverberation Mapping with Meter-Class Telescopes" (2015). *Theses and Dissertations*. 5469.
<https://scholarsarchive.byu.edu/etd/5469>

This Thesis is brought to you for free and open access by BYU ScholarsArchive. It has been accepted for inclusion in Theses and Dissertations by an authorized administrator of BYU ScholarsArchive. For more information, please contact scholarsarchive@byu.edu, ellen_amatangelo@byu.edu.

A Feasibility Study of Photometric Reverberation Mapping with Meter-Class Telescopes

Carla June Carroll

A thesis submitted to the faculty of
Brigham Young University
in partial fulfillment of the requirements for the degree of
Master of Science

Michael Joneer, Chair
Eric Hintz
Denise Stephens

Department of Physics and Astronomy
Brigham Young University
June 2015

Copyright © 2015 Carla June Carroll

All Rights Reserved

ABSTRACT

A Feasibility Study of Photometric Reverberation Mapping with Meter-Class Telescopes

Carla June Carroll
Department of Physics and Astronomy, BYU
Master of Science

For the past several decades, mass estimates for supermassive black holes hosted by active galactic nuclei (AGN) have been made with the reverberation mapping (RM) technique. This methodology has produced consistent results and has been used to establish several relations that link the characteristics of the host galaxy to the mass of the central black hole. Despite this success, there are less than 50 AGN with black hole masses derived from RM. This low number is generally attributed to the difficulties in coordinating large blocks of telescope time for making simultaneous photometric and spectroscopic observations. Spectroscopic observations also generally require several months of nightly observations with moderate to large size telescopes as the signal-to-noise ratio is too low for smaller telescopes.

We have made photometric observations of NGC 5548 in four filters (a custom-made $H\alpha_{10}$ filter, the Strömgren y filter, the Johnson/Cousins V filter and the Johnson/Cousins R filter) in order to evaluate a photometric methodology for determining the lag time between the variations observed in the continuum and the $H\alpha$ emission from the broad-line region (BLR) gas. This time delay represents the mean light travel time to the BLR and is therefore a measurement of the mean BLR radius. Multiple JAVELIN analyses of the three continuum light curves (y , V , and R), relative to the light curve from the $H\alpha_{10}$ filter yields a value for $\tau = 3.3 \pm 0.1$ days. Adopting a value of $f = 5.5$, along with a single-epoch spectroscopic measurement from Park et al. (2012) of $\Delta v = 4354 \pm 25$ km/s, enables us to estimate a black hole mass of $M_{\text{BH}} = 67.2 \pm 2.2 \times 10^6 M_{\odot}$.

Keywords: reverberation mapping, supermassive black holes, NGC 5548, active galactic nuclei

Contents

Table of Contents	iii
1 Introduction	1
1.1 Measures of Supermassive Black Hole Mass	1
1.2 Historical Background	2
1.3 Active Galactic Nuclei	2
1.4 Traditional Reverberation Mapping	8
1.5 Traditional vs. Photometric	10
1.6 Dependency of f	11
2 Methods	13
2.1 Photometric Filters	13
2.2 Observations	14
2.3 Image Processing	16
2.4 Photometry	18
2.5 Cross-correlation Analysis	27
2.6 Obtaining Archival Velocity Dispersion	30
3 Results and Discussion	32
3.1 Review of Goal	32
3.2 Data Acquisition	32
3.3 Analysis	36
3.4 Calculations	44
3.5 Further Work	44
Appendix A Data Tables	46
Bibliography	58

Chapter 1

Introduction

1.1 Measures of Supermassive Black Hole Mass

Most massive galaxies contain supermassive black holes (SMBHs) in their nuclei, with $M > 10^6 M_{\odot}$. These SMBHs may originate from massive primordial stars and grow through cosmic time via mergers with other BHs, accretion and other processes. Because the nuclei in which they reside are dense with stars it is very difficult to resolve them, so observation can tell us little about their internal structure or how they formed and evolved.

Estimates of SMBH masses are made either through direct or indirect measurements. Direct measurements derive SMBH masses from the dynamics of stars or gas accelerated by the black hole via stellar and gas modeling or reverberation mapping. Indirect measurements rely on correlations between SMBH masses and their host galaxy bulges such as the M - σ^* relation of the velocity dispersion within an AGN's bulge and its associated central SMBH mass (Ferrarese & Merritt 2000; Gebhardt et al. 2000; Tremaine et al. 2002), the SMBH mass-bulge luminosity relationship (Kormendy & Richstone 1995) and other AGN scaling relationships like those by Bentz et al. (2009a). Another direct measurement method is radio analysis of mass outflow from

multiple masers (*microwave amplification by stimulated emission of radiation*), which requires high spatial resolution. This method is very accurate, but requires the existence of a maser close enough to the center of the galaxy to resolve velocities, which is rare. To determine the mass function of SMBHs and better correlate their properties with those of their host galaxies, a method of obtaining much larger samples of SMBH masses is needed.

1.2 Historical Background

In the 1930s, Carl Seyfert found that about 10% of all galaxies had a bright, stellar-like nucleus. Over the following decades, as our understanding and description of galaxies evolved, especially those of active galactic nuclei, it was found that these bright nuclei did not have a dominant stellar spectra. Stellar sources essentially have a blackbody spectral energy distribution (SED) but AGN emit much more energy over a larger range of wavelengths. Stellar sources also exhibit absorption spectral lines while an AGN has emission spectra features. Advances in radio astronomy later led to the discovery of other highly luminous extragalactic sources (Shields 1999). Subsequent spectroscopic observations found that some of these bright nuclei had broadened emission lines. In the 1960s similar broadened emission was found in seemingly stellar objects but displaced to high redshifts, suggesting that they are moving away from us at high velocities. They were later named quasi-stellar objects (QSOs), or quasars, and classified as distant Seyfert galactic nuclei with higher luminosities. Quasars were studied for some time before their high redshift nature was realized.

1.3 Active Galactic Nuclei

Active galaxies have an energy source at their center (or bulge) that emits radiation that cannot be attributed to stars. The flux usually has a high energy tail that can be represented as a power law in

frequency. It is thought to be due to synchrotron emission of mass being accreted onto a SMBH. This central region, called an AGN, is generally compact, only light hours or light days across, and in some cases is comparable in size to our solar system. Most massive galaxies are believed to contain SMBHs but are only classified as active if the black hole is accreting, since each inflow of matter creates a flare in luminosity. Objects classified as AGN include quasars, blazars, and Seyfert galaxies.

The current model for AGN, illustrated in Fig. 1.1, is a black hole at the center of an accretion disk with rapidly rotating material. Relatively close to the center of the disk is the broad-line region (BLR) where fast outflows ($v_{FWHM} > 800$ km/s) Doppler broaden the lines (mainly hydrogen). Previously, AGN were classified as distinct objects based on their spectral features, such as blazars (variable high energy sources) and Seyferts. The AGN unification model shown in Fig. 1.1 clarifies that these sources are actually the same structure viewed from different angles. If the jet is viewed end on, it is a blazar. Viewed from other angles, it becomes a Seyfert 1 or 2 galaxy. Note that the Seyfert 1 viewing angle allows the observer to see the BLR, while in a Seyfert 2 only the narrow-line region (NLR), whose lines are much less broadened, is visible. Velocity measures in the NLR, however, do not give the kinematic information needed for the velocity dispersion measurement without the broader emission lines from the BLR. As seen in Fig. 1.1, the NLR is at a much larger distance from the black hole and thus has a much lower dispersion velocity.

Absolute magnitudes for AGN or quasars can exceed $M_B = -23.5$ or $2.15 \times 10^{11} L_{\odot}$, making them optically the brightest objects in the universe. This luminosity comes from outbursts as the material collides on the accretion disk as it spirals inwards around the SMBH at the core of the nucleus. Although such material can be of any size and is likely to be quite small, the energy emitted from such collisions will result in high energy outbursts. The SEDs of AGN are variable due to the sporadic nature of the accretion. Although this variability is a distinguishing characteristic of AGN and comprises almost all the luminosity, their variability can also result

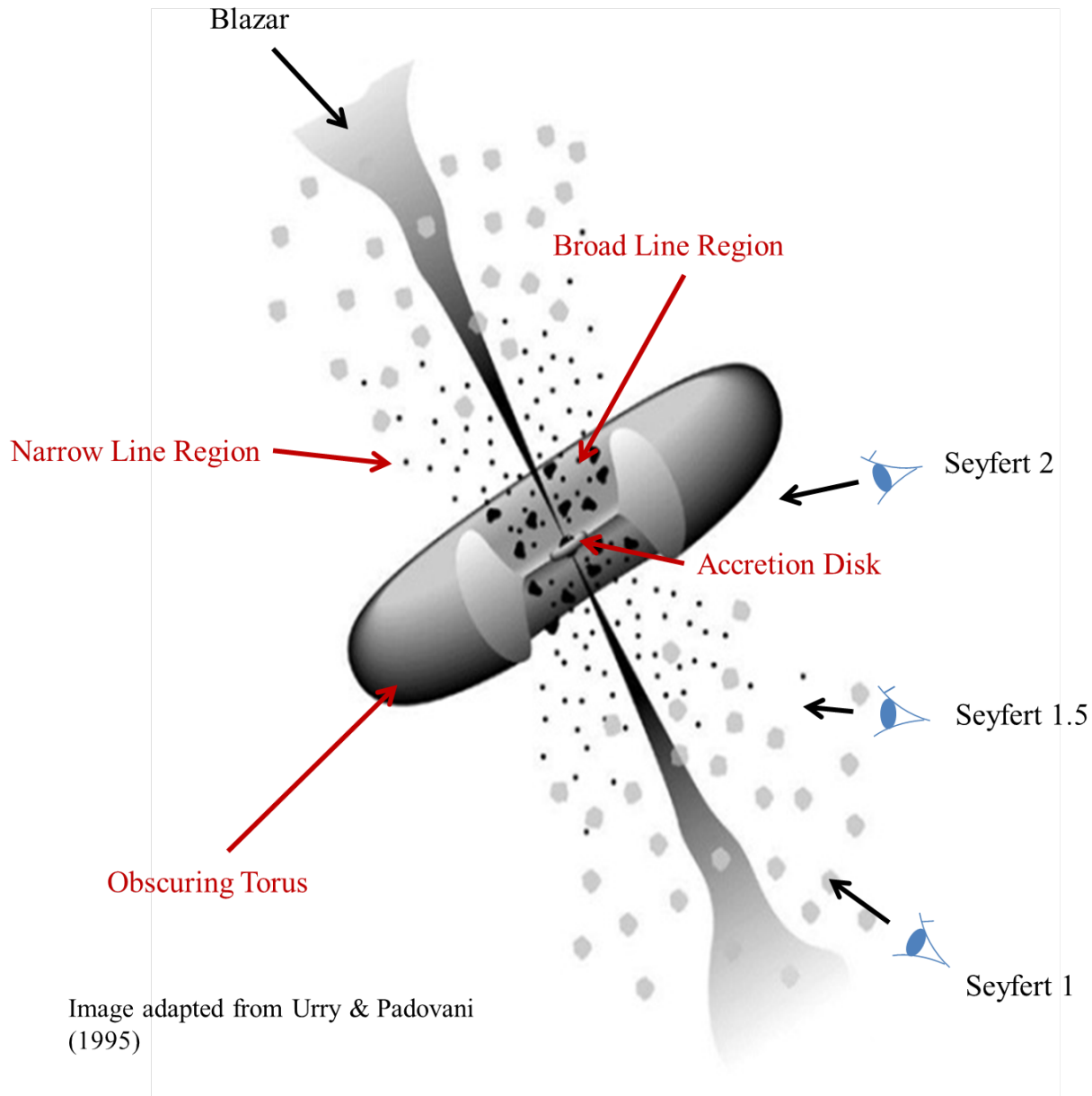


Figure 1.1 In the Unified Model, different types of AGN are just a SMBH surrounded by an accretion disk that is viewed at different angles. The black hole is shown at the center of the disk with rapidly rotating material. The broad-line region (BLR) is close to the disk. From Urry & Padovani (1995).

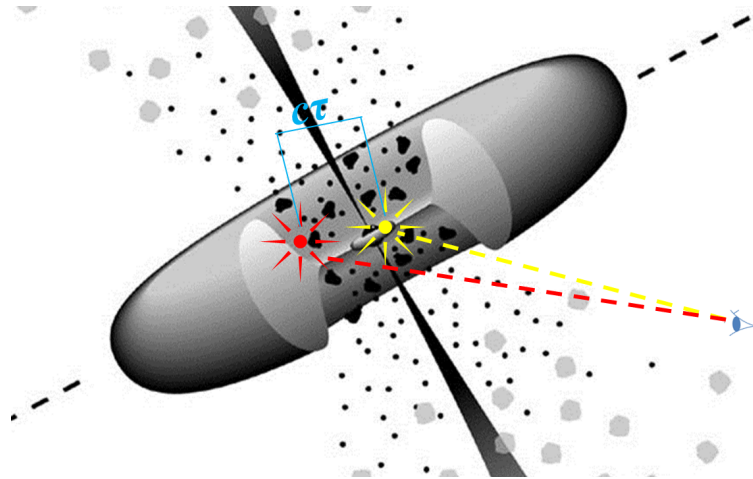


Figure 1.2 Light radiates first from the central region of the AGN in all directions (yellow). After a few hours/days of travel, some of the photons will interact with material in the broad-line region, or BLR (see Fig. 1.1), which will absorb and re-emit the light (red). Radiation from the two sources is detected with a time lag, which gives the BLR radius, $c\tau$. This is like sound echoing from a wall, hence the term “reverberation mapping”. From Urry & Padovani (1995).

from supernovae, starbursts and microlensing. The optical flux can vary on timescales of days or even hours in some cases. Such rapid variability indicates the emitting source is extremely small.

To illustrate this point, consider an instantaneous flash from a spherical object, as shown in Fig. 1.2 (also see Fig. 1.3 and Fig. 1.4). Light radiates first from the central region of the AGN in all directions (in yellow). This burst propagates in all directions and some of the light is absorbed and then re-emitted by gas in the BLR just a few light hours or light days distant (re-emitted burst shown in red in Fig. 1.2). Since this gas is (usually) a few light days from the accretion disk, reprocessed light from the BLR would first appear a few hours or days after the initial flare. Given that the object is optically thick to allow sufficient reverberation, the radius of the BLR can then be determined from $R = c\tau$ as shown in Fig. 1.2. The luminosities of Seyfert-type AGN commonly vary over days or hours, implying that the broad-line source must be less than several light hours across. Reverberation mapping techniques assume that the source of broad line emission is no larger than a few light hours.

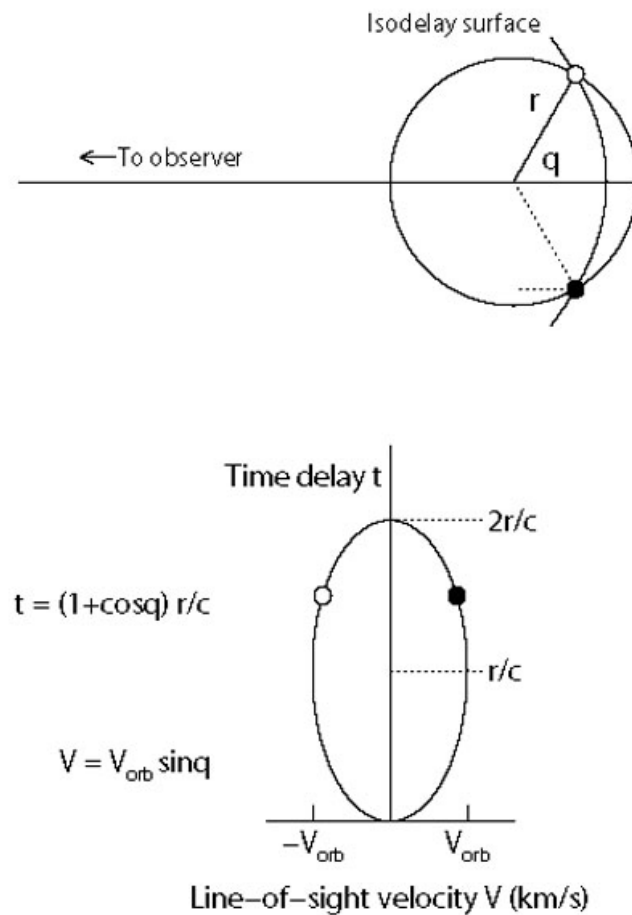


Figure 1.3 The upper diagram shows the structure of the AGN with fast-moving clouds around the core to give an observer’s perspective of the time lag (with the observer on the left). This gives the ideal case of the “isodelay surface” to which the time delay relative to the continuum signal will be $\tau = (1 + \cos q)r/c$ as shown on the dotted line. The angle q is the angle between the solid line and the dotted line. The radius r is the BLR radius $c\tau$ as shown in Fig. 1.2. The lower diagram shows a circular orbit mapped into the line-of-sight velocity/time-delay plane (Peterson & Horne 2004).

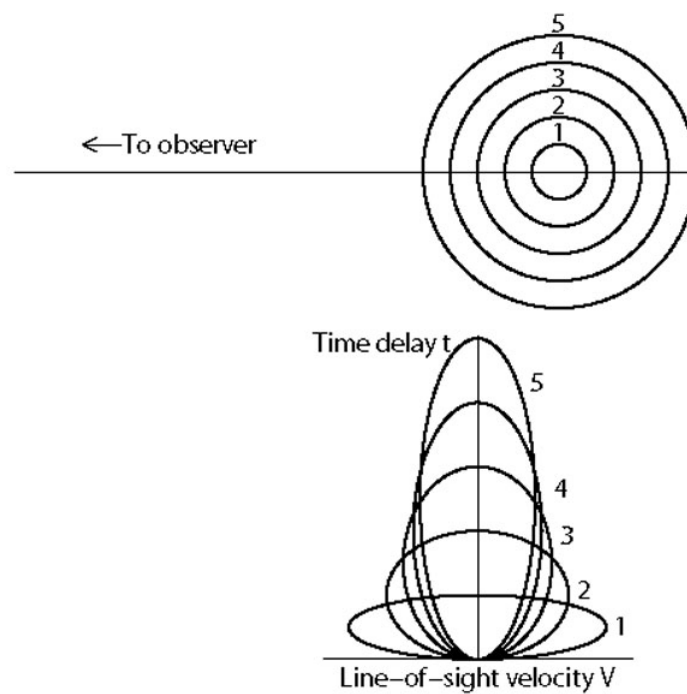


Figure 1.4 Similar to Fig. 1.3 but seen from a different angle. This image gives a different view of how Keplerian orbits would appear on the velocity-time delay phase. (Peterson & Horne 2004).

A simplified geometry of an “isodelay surface” (see Fig. 1.3) gives another perspective of the bursts as they occur from the viewpoint of the observer as well as a circular orbit mapped into the line-of-sight velocity/time-delay plane. Potential inclination angles are described in Fig. 1.4 (Peterson & Horne 2004). These figures illustrate how the geometry of an AGN can impact the results of a reverberation mapping project.

1.4 Traditional Reverberation Mapping

The primary goal of reverberation mapping is to probe the structure and kinematics of the BLR through observations of the Doppler-broadened emission lines against the continuum (Peterson & Horne 2004). There is a simple relation between the observed continuum emitted as an initial light burst from the accretion disk and the ionizing continuum resulting from the re-emitted burst in the BLR. This relation is derived naturally from the phase difference. As described by Peterson & Horne (2004),

"a linearized approximation response model can be written as

$$\Delta L(V, t) = \int \Psi(V, \tau) \Delta C(t - \tau) d\tau$$

where $\Delta C(t)$ is the continuum light curve relative to its mean value \bar{C} , i.e., $\Delta C(t) = C(t) - \bar{C}$, and $\Delta L(V, t)$ is the emission-line light curve as a function of line-of-sight Doppler velocity V relative to its mean value $\bar{L}(V)$. The function $\Psi(V, \tau)$ is the velocity-delay map, i.e., the BLR responsivity mapped into line-of-sight velocity/time-delay space."

Closer examination of this velocity-delay map shows that it is just the response of the BLR to a delta function outburst from the accretion disk.

This technique assumes that the AGN in the standard model (Fig. 1.1) obeys the relationship between black hole mass and host-galaxy bulge velocity dispersion (Merritt et al. 2001). If not,

the black hole mass and host-galaxy bulge velocity dispersion would need to be corrected for bias for the approximations assumed in reverberation mapping to be valid.

The radius of the broad-line region can be found from its variability (Fig.1.2). Given a virialized system, we can assume $-2K = U$, where U is the gravitational potential energy of the gas clouds in the BLR, $U = -G\frac{M_{\text{BH}}m}{r_{\text{BLR}}}$ and K is the kinetic energy, $K = \frac{1}{2}m\Delta v^2$, where Δv is the velocity dispersion within the BLR. This yields a virial mass estimate,

$$M_{\text{BH}} = f \frac{\Delta v^2 c \tau}{G},$$

where f is a scaling factor, Δv is the Doppler broadening velocity, $c\tau$ is the radius of the BLR and G is the gravitational constant.

Reverberation mapping requires spectroscopic and imaging data for velocity dispersion and variability measurements, respectively. This variability is not expected to be periodic, as is typical of many variable stellar sources. Rather, AGN emission varies erratically on timescales of days or even hours. This variation is generally attributed to material falling onto the accretion disk as mentioned above, or perhaps from instabilities in the magnetic field structure. Regardless of the origin of variability, a continuum brightening is followed by an increase in the broad-line emission flux with a lag of several days or weeks. We estimate the diameter of the BLR as $c\tau$, as shown in Fig. 1.2.

Besides masers, reverberation mapping is another well-established method for estimating SMBH mass, although the need for spectroscopy generally requires telescopes of at least two meters in diameter. Such large telescopes are expensive and require a long application process and a measure of luck (e.g. timing against competing observers, connections, etc.). Such a process involves applying for time on the telescope and hoping that no weather, technical mishaps or other conditions stand in the way when/if time is granted. Even if an application for time on a large telescope successfully goes through without any issue, the AGN may be quiescent during the observed time, eliminating the needed variability for reverberation mapping to succeed. Because

of this barrier, only ~50 AGN have been reverberation mapped, giving a very small sample size for theorists to work with for use in gaining a better understanding of SMBH characteristics and probing dark energy (Haas et al. 2011; Watson et al. 2011). Given that there are thousands if not millions of AGN that could be decent candidates for reverberation mapping, this sample size is rather low.

1.5 Traditional vs. Photometric

Photometric reverberation mapping is a recent innovation to traditional reverberation mapping. It efficiently estimates the black hole mass, putting a greater weight on statistical analysis and less on spectral data. There are a few different options within photometric reverberation mapping, such as broadband and narrowband photometric reverberation mapping. Broadband photometric reverberation mapping covers a greater range of wavelengths, using filters that are commonly accessible to many universities and other organizations, such as public observatories. Narrowband photometric reverberation mapping is a similar method that accesses spectral features by only observing in a wavelength range that just covers the spectral feature. Each filter must be fit to the redshift of each galaxy. Since each filter samples an emission line within a limited range of redshift space, multiple expensive filters would be required to observe targets with a wide range of redshifts.

The accuracy of broadband photometric reverberation mapping relative to photometric reverberation mapping is discussed by Chelouche & Daniel (2012), who performed a feasibility study with numerical simulations and found that line-to-continuum time delays associated with the BLR in AGN can be deduced from broadband light curves. The light curves are analyzed in comparison with each other to determine a lag time as described above. They applied their method to the Palomar-Green quasar sample, which had spectroscopic reverberation mapping results for com-

parison. They found agreement between the accurate spectroscopic results and their photometric counterparts. Another example of broadband photometric reverberation mapping is from Edri et al. (2012). Edri et al. used a lower luminosity source, NGC 4395, allowing them to determine a lag time on the order of hours instead of days or months, maximizing the short telescope time they were allotted. These two studies show that broadband photometric reverberation mapping provides a simplified observational approach to reverberation mapping without loss of accuracy.

The goal of our project is to estimate the mass of the SMBH in NGC 5548 from data taken with the WMO 0.91 meter (meter-class) telescope in the 2014 observing season and from archival velocity dispersion measurements. In our present study of NGC 5548, we emphasize the use of broadband filters (see Table 2.1) for continuum emission and intermediate-band filters (see Table 2.2) for the $H\alpha$ emission line. Since the goal of our study was to create more efficient and affordable estimates of SMBH masses, we note that the intermediate-band filters in our work were reasonably priced and would be within the budget of most universities. We chose Strömgren y and $H\alpha_{10}$ filters, which are intermediate-band filters, because a narrower filter would have excluded regions of the $H\alpha$ emission line. We also used the Johnson/Cousins V and R broadband filters for an additional continuum measure.

1.6 Dependency of f

The constant f is a measure of the composition and state of the emitting gas, the geometry of the nucleus of the AGN, and its inclination angle. The value of f that should be used in the reverberation mapping equation remains a topic of debate. In the early days of reverberation mapping, Peterson & Horne (2004) proposed that f should be on the order of unity. The first calibration of f was by Onken et al. (2004), who found $f = 5.5 \pm 1.8$ from a sample of 14 AGN that had been previously reverberation mapped. In the last 10 years, mass estimates using $f = 5.5$

and $f = 1$ have become standard in the community. Efforts are being made to model reverberation mapping data in order to constrain the geometry and dynamics of the BLR (Pancoast et al. 2014). In other recent work, reverberation mapping campaigns using $H\beta$ as the emission source and Seyfert 1 – 1.5 type galaxies found $f \sim 2.5 - 5.5$ (Bentz et al. 2007; 2009b; 2010; Park et al. 2012; Woo et al. 2010). For more specific values of f in recent literature, see Section 2.6. As the the most common value given for f in recent work is $f = 5.5$, we adopt this value in our analyses.

Chapter 2

Methods

2.1 Photometric Filters

This project began in 2012 exclusively with broadband filters to observe one AGN, Mrk 926 (see Table 3.1). During the three months of data acquisition, Mrk 926 was relatively quiescent so we were unable to attempt a black hole mass estimate. We used the Johnson/Cousins set: the B filter, centered at 445 nm and $\Delta\lambda = 94$ nm; the V filter, centered at 551 nm and spanning 88 nm; the R filter, centered at 658 nm with $\Delta\lambda = 138$ nm; and the I filter, with $\lambda_{\text{eff}} = 806$ nm and $\Delta\lambda = 149$ nm (Table 2.1). In 2013, we observed five additional AGN: KA 1858, Mrk 50, Mrk 817, NGC 4051 and Zw 229, with additional narrowband and intermediate-band filters (WA centered at 656 nm with a $\Delta\lambda = 20$ nm and NA also centered at 656 nm with a $\Delta\lambda = 3$ nm as shown in Table 2.1). Observations in 2014 with custom intermediate-band filters with a bandpass of about 20-nm yielded measurements of time-varying emission in $H\alpha$ along with the continuum (Table 2.2, Fig. 2.1).

The general method for obtaining black hole masses by photometric reverberation mapping requires one filter for the desired emission feature and another filter for the continuum (shown

for NGC 5548 in Fig. 2.1). Our intent was to test if we could isolate contributions from variable emission lines relative to continuum-only measurements provided from a filter free of dominant emission features. In comparison to traditional reverberation mapping, the photometric technique utilizes archival spectra to estimate the velocity dispersion from the Doppler-broadened lines from the BLR of the AGN. Many AGN are faint enough that, in order to monitor the changes in flux from the broad-line reverberation, it is necessary to secure spectra and then integrate the flux in the broad lines semi-continuously over periods of several months, depending on the size of the lag time. Spectroscopic observations require much larger telescopes than photometric observations of the same objects. We note that the position of the relative BLR will vary slightly in time due to the level of outburst that is coming out of the nucleus. However, this is a secondary effect and should not impact an estimate derived from a photometric technique and a single epoch spectrum.

2.2 Observations

We used data from the 2014 observing season to evaluate the feasibility of a photometric reverberation mapping method with a meter-class telescope. Observations were taken in the filters listed in Tables 2.1 and 2.2 on the 0.91-meter $f/5.5$ Cassegrain telescope at WMO. All filters listed in Table 2.2 were available and could be used to observe the AGN in our campaign at their respective redshifts, although only the $H\alpha_{10}$ was used for NGC 5548. $H\alpha_{00}$, $H\alpha_{20}$ and $H\alpha_{40}$ were also used for other AGN during the same observing season. The data were processed with the Image Reduction and Analysis Facility (IRAF), using AstroImageJ for aperture photometry with R, Matlab and JAVELIN for the time lag analysis thereof.

In observations highlighting the emission feature, the light curve showing the variability is a convolution of flux from the continuum measurement and the variability from the emission feature. The light curves produced are similar to those one would obtain from spectral data with very

Table 2.1 Filters currently available at WMO. The Johnson/Cousins broadband filter set and the Strömgren intermediate-band filters were primarily used for continuum measurements according to the best fit for each AGN. The narrowband filter sets ($\Delta\lambda \leq 5$ nm) and the selected intermediate bands listed highlight the $H\alpha$ and $H\beta$ emission features at zero redshift.

Name	λ_{eff}	$\Delta\lambda$	Name	λ_{eff}	$\Delta\lambda$
Sloan			Strömgren		
u'	352 nm	65 nm	u	350 nm	30 nm
g'	475 nm	150 nm	v	410 nm	16 nm
r'	630 nm	133 nm	b	470 nm	19 nm
i'	795 nm	149 nm	y	550 nm	24 nm
z'	873 nm	94 nm	$H\beta$		
Johnson/Cousins			WB	486 nm	15 nm
B	445 nm	94 nm	NB	486 nm	3 nm
V	551 nm	88 nm	$H\alpha$		
R	658 nm	138 nm	WA	656 nm	20 nm
I	806 nm	149 nm	NA	656 nm	3 nm

Table 2.2 Filters at West Mountain Observatory after April 2014. Maximized results for each object are obtained with filters that are centered on $H\alpha$ at the redshift of the object.

Filter	λ_{eff}	$\Delta\lambda$	Redshift Range
$H\alpha_{00}$	656.3 nm	20 nm	$0 < z < 0.009$
$H\alpha_{10}$	667 nm	21 nm	$0.009 < z < 0.024$
$H\alpha_{20}$	677 nm	21 nm	$0.024 < z < 0.039$
$H\alpha_{30}$	687 nm	21 nm	$0.039 < z < 0.054$
$H\alpha_{40}$	697 nm	21 nm	$0.054 < z < 0.070$
$H\alpha_{50}$	707 nm	21 nm	$0.070 < z < 0.085$
$H\alpha_{60}$	717 nm	21 nm	$0.085 < z < 0.100$

little continuum. We hope to eventually generalize this method to include broadband filters (e.g. Johnson/Cousins in Table 2.1) to find a statistically significant measurement with low error measurements to further study several AGN that have already been observed (see Table 3.1) and more fully investigate the feasibility of photometric reverberation mapping with meter-class telescopes. As discussed later, these filters were originally proposed for a more extensive project. We used the $H\alpha_{10}$ filter to capture $H\alpha$ line emission from NGC 5548 and the Strömgren y, Johnson/Cousins V and R filters for continuum measurements.

2.3 Image Processing

We used IRAF for all reductions of NGC 5548 to produce processed frames from raw images. We used the standard image calibration process involving bias and dark and flat images for corrections to an object frame. The bias image is taken by simply reading the CCD after making a zero length exposure. These images correct the zero level of the frame to account for the amplifier bias as the image is read from the CCD sensor. The next calibration frame needed is a dark frame, which is an

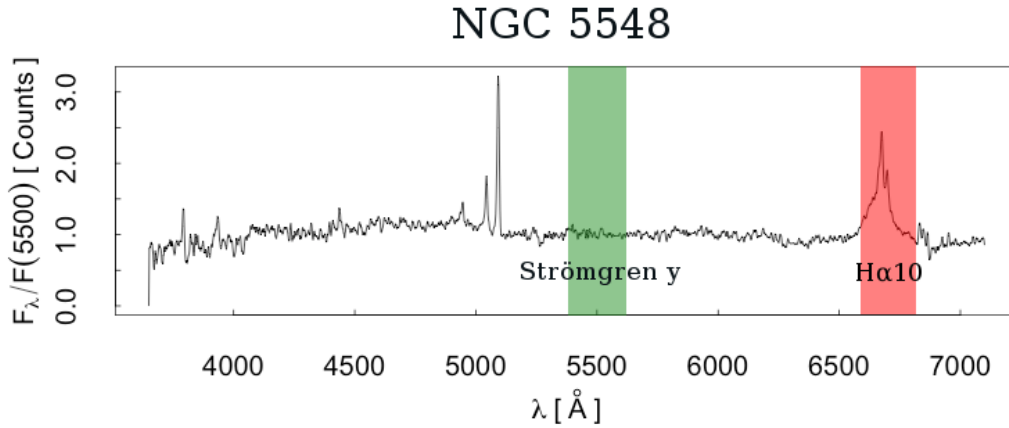


Figure 2.1 Archival spectra of NGC 5548 from the NASA/IPAC Extragalactic Database (NED) superimposed on the wavelength ranges of the intermediate-band Strömgen y filter and intermediate-band filter $H\alpha_{10}$ (see Tables 2.1 and 2.2).

image taken with the CCD shutter closed in order to avoid capturing any external light during the exposure. This allows for a correction for dark current, which consists of the electrons present in every CCD sensor at typical working temperatures due to thermal excitations rather than incident photons during an exposure. Finally, since CCD pixels each have a slightly different response, flat frames are taken to normalize the pixel responses. There are methods for securing flat field calibration frames, including placing a light box at the end of the telescope, a white screen attached to the end of the telescope, and aiming the telescope at a section of plain sky during dusk or dawn. At WMO the latter is done, using a patch of cloudless sky, usually at dusk.

The corrections made with these frames must be done in the proper order. Each correction is made in IRAF, applying the final element of each procedure to the next. The correction can be summarized in a formula,

$$\text{Final Image} = \frac{\text{Raw Image} - (\text{Dark Frame} - \text{Bias Frame})}{\text{Flat Frame}}.$$

In other words, the combined bias frame is first subtracted from the combined dark frame. The result is then subtracted from the raw image. The product of these two operations, the numerator in

the above formula. is then divided by the combined flat frame for each filter. The calibrated frames are the result of either subtracting or dividing each program frame pixel by pixel. All frames are also overscan corrected to remove the instantaneous bias level of each exposure. This procedure ensures that any time-dependent drift in the bias level is corrected relative to the overscan strip that is sampled along with each program exposure.

2.4 Photometry

We performed aperture photometry within AstroImageJ (Collins & Kielkopf 2013), an image processing program customized for astronomy from the generic ImageJ, on NGC 5548 to determine differential flux. This flux is relative to several field stars that are confirmed to be constant over time and can thus provide a consistent comparison ensemble from night to night. Aperture photometry subtracts the total photon count within a fixed inner circular aperture to give an approximation to the point-spread function (PSF) of each object. We used a multi-aperture option within AstroImageJ. This includes an object aperture and a background annulus with user-specified radii. This process takes the photon count within the object aperture and eliminates the background sky counts by subtracting the photon count per pixel as determined from the sky annulus. Aperture photometry is done from the user's perspective by selecting objects (stars or point-like galaxies) in images such as Figs. 2.2– 2.5 in AstroImageJ. The constant comparison stars serve as a baseline to allow a differential solution for the total photon counts within each object's aperture.

AstroImageJ provides the option in photometry for either a fixed aperture or a variable aperture based on the full width at half maximum (FWHM) measurement of the main target object. The multiplication factor can be specified by the user. We performed photometry with each filter with both fixed and variable apertures (with 1.40 times the measured FWHM). With the fixed apertures we used the following parameters: radius of object aperture=10, inner radius of background an-

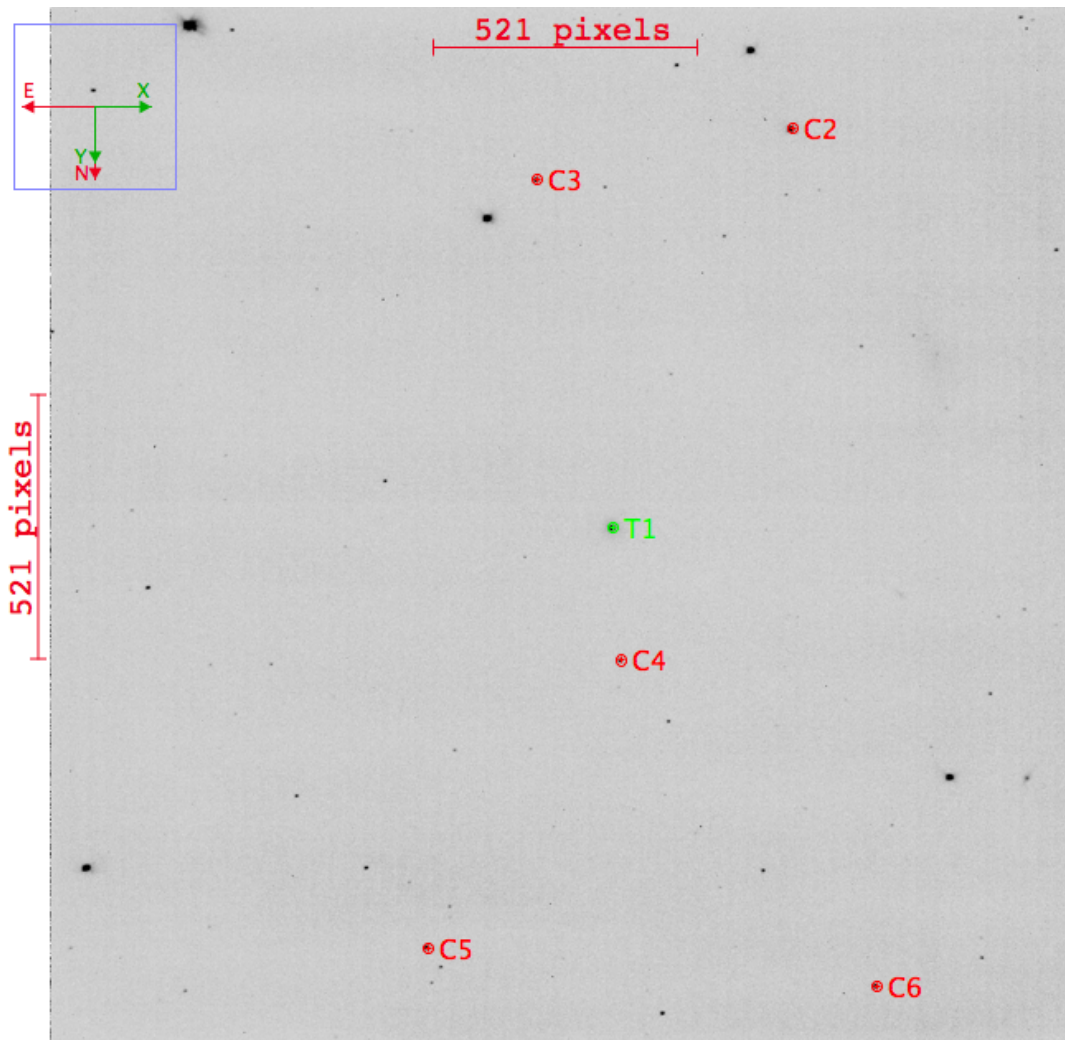


Figure 2.2 A typical image from WMO in the $H\alpha_{10}$ filter after basic processing. NGC 5548 is marked in the middle (T1) and the numbered stars indicate the comparison stars. Comparison stars varied slightly between the different filters. As our method of photometry produces a differential solution, slightly different comparison stars do not affect the NGC 5548 light curves. Fig. 2.6 shows the variability analysis for the comparison stars in the $H\alpha_{10}$ filter. This image has a $20.8'$ square field of view.

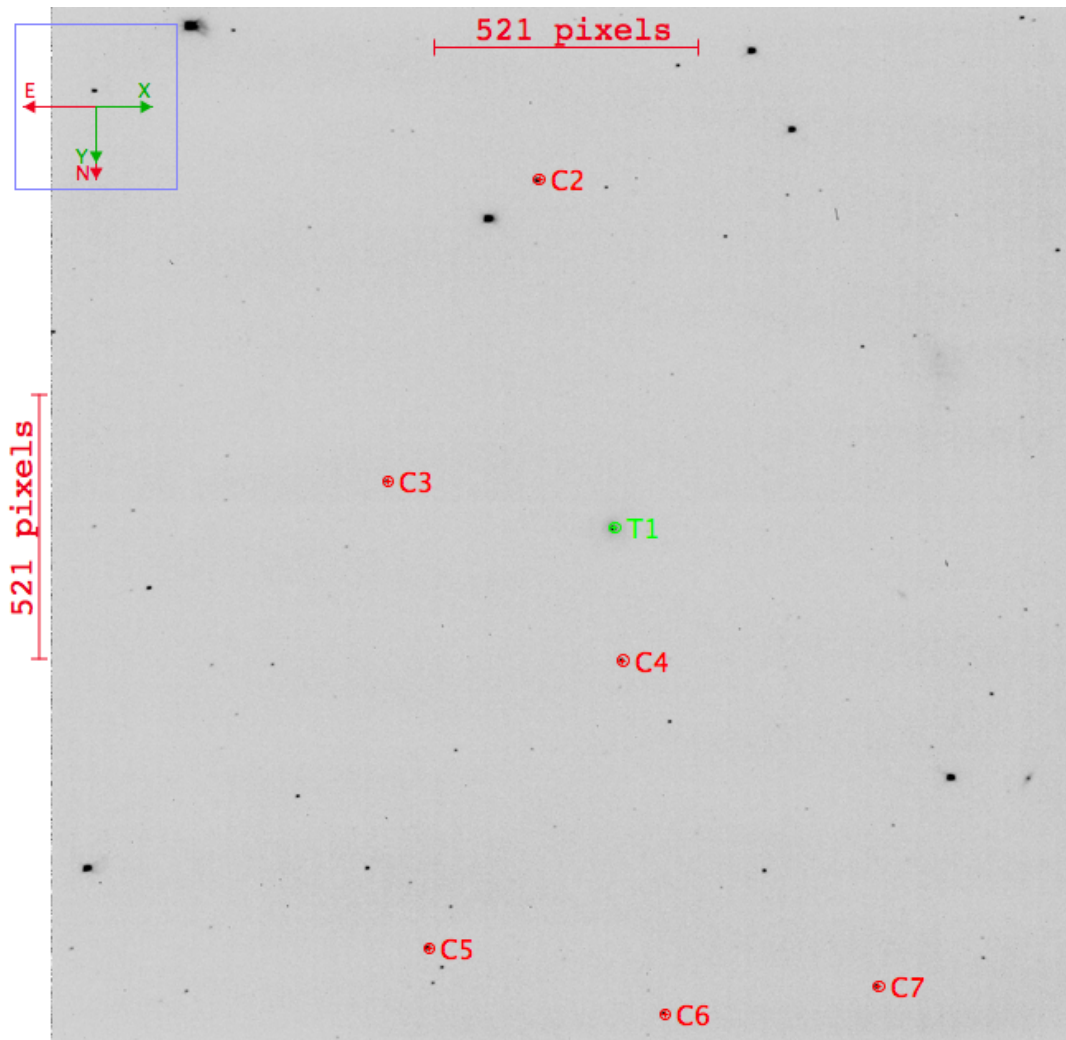


Figure 2.3 A typical image from WMO in the Strömgren y filter after basic processing. NGC 5548 is marked in the middle (T1) and the numbered stars indicate the comparison stars. Comparison stars varied slightly between the different filters. As our method of photometry produces a differential solution, slightly different comparison stars do not affect the NGC 5548 light curves. Fig. 2.7 shows the variability analysis for the comparison stars in the Strömgren y filter. This image has a 20.8' square field of view.

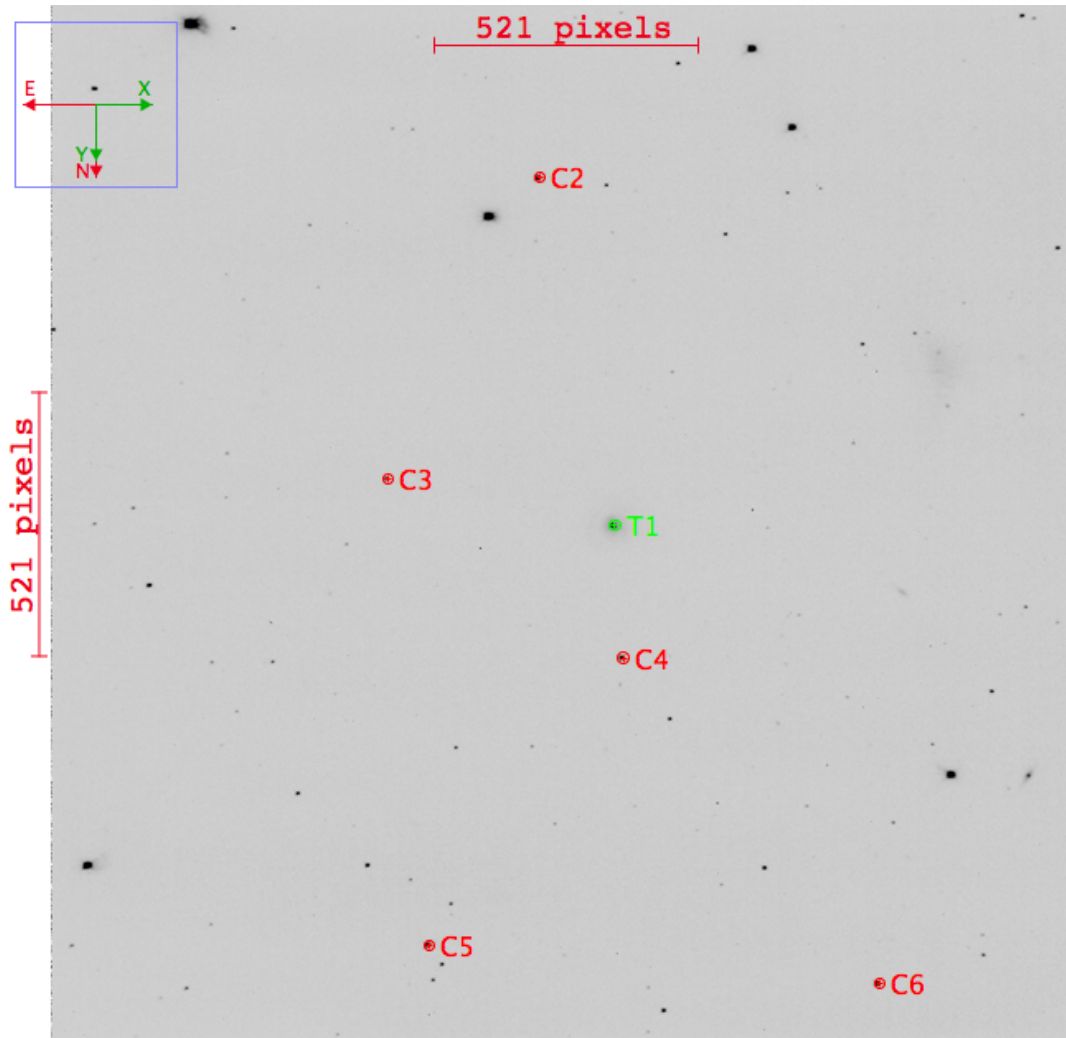


Figure 2.4 A typical image from WMO in the Johnson/Cousins V filter after basic processing. NGC 5548 is marked in the middle (T1) and the numbered stars indicate the comparison stars. Comparison stars varied slightly between the different filters. As our method of photometry produces a differential solution, slightly different comparison stars do not affect the NGC 5548 light curves. Fig. 2.8 shows the variability analysis for the comparison stars in the Johnson/Cousins V filter. This image has a 20.8' square field of view.

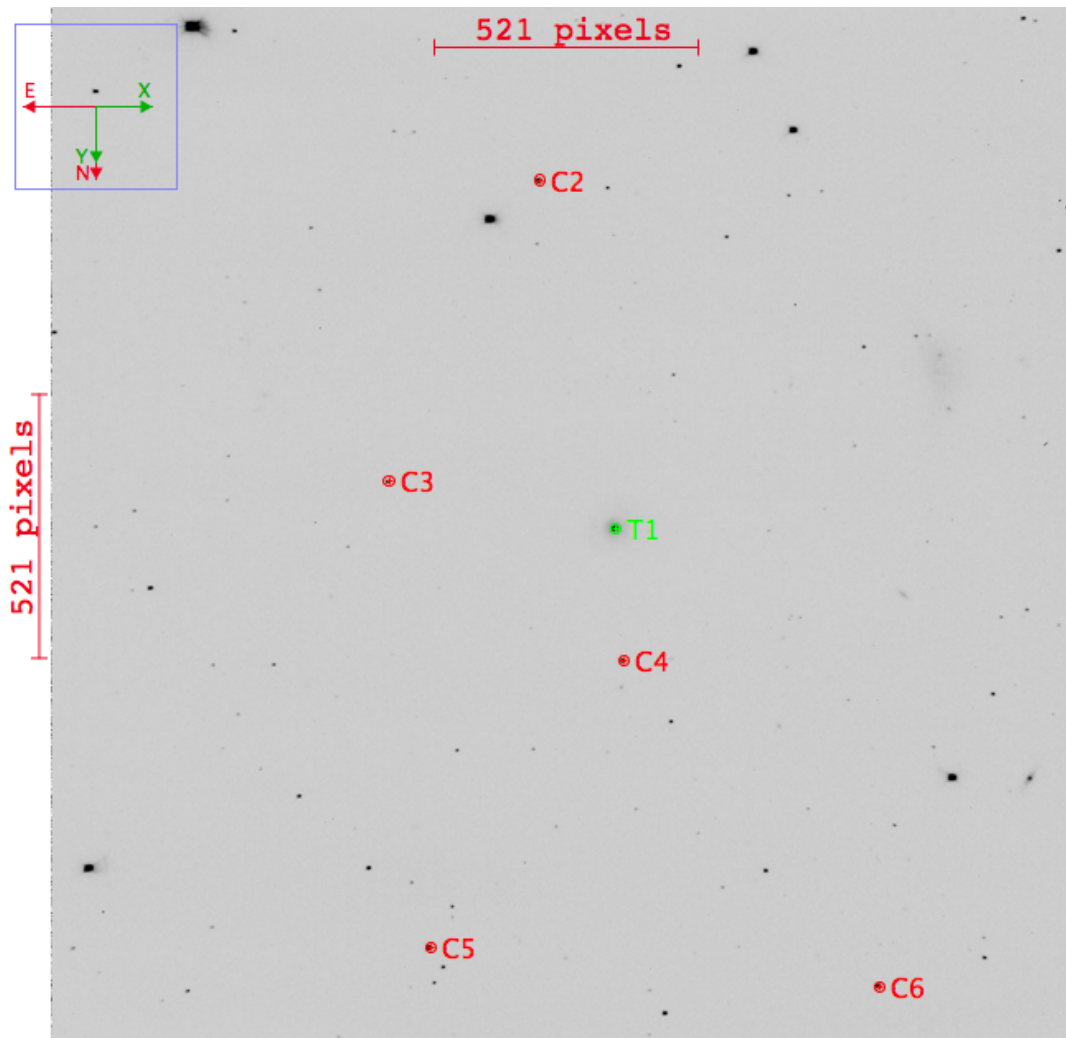


Figure 2.5 A typical image from WMO in the Johnson/Cousins R filter after basic processing. NGC 5548 is marked in the middle (T1) and the numbered stars indicate the comparison stars. Comparison stars varied slightly between the different filters. As our method of photometry produces a differential solution, slightly different comparison stars do not affect the NGC 5548 light curves. Fig. 2.9 shows the variability analysis for the comparison stars in the Johnson/Cousins R filter. This image has a 20.8' square field of view.

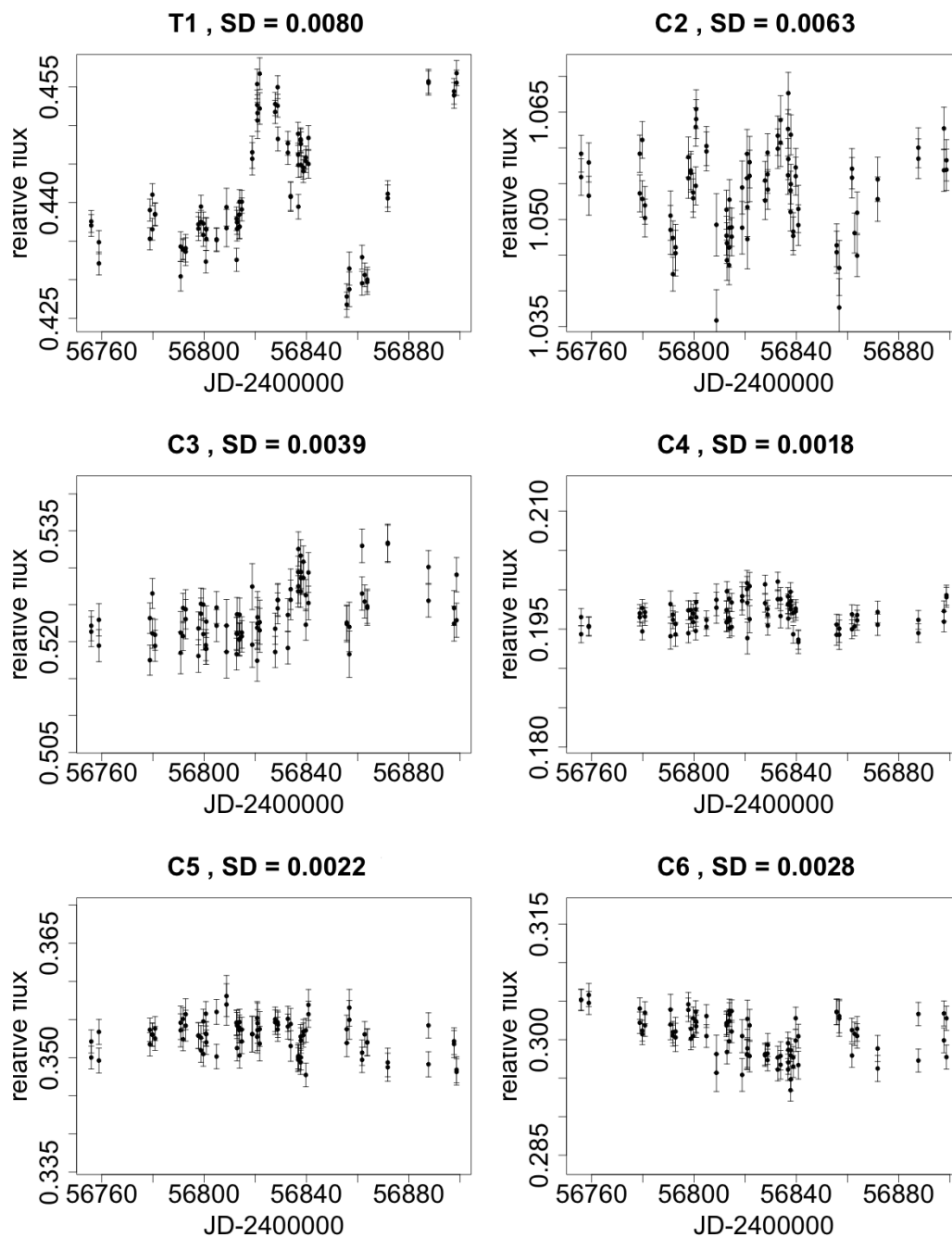


Figure 2.6 Comparison star light curves from the $H\alpha_{10}$ filter to check for significant variability. The label SD at the top of each plot indicates the standard deviation. T1 is the AGN. C2 was quite variable and thus removed as a comparison star. All comparison star plots were adjusted to the same span of relative flux as was given by NGC 5548 (T1). The marked comparison stars are shown in Fig. 2.2.

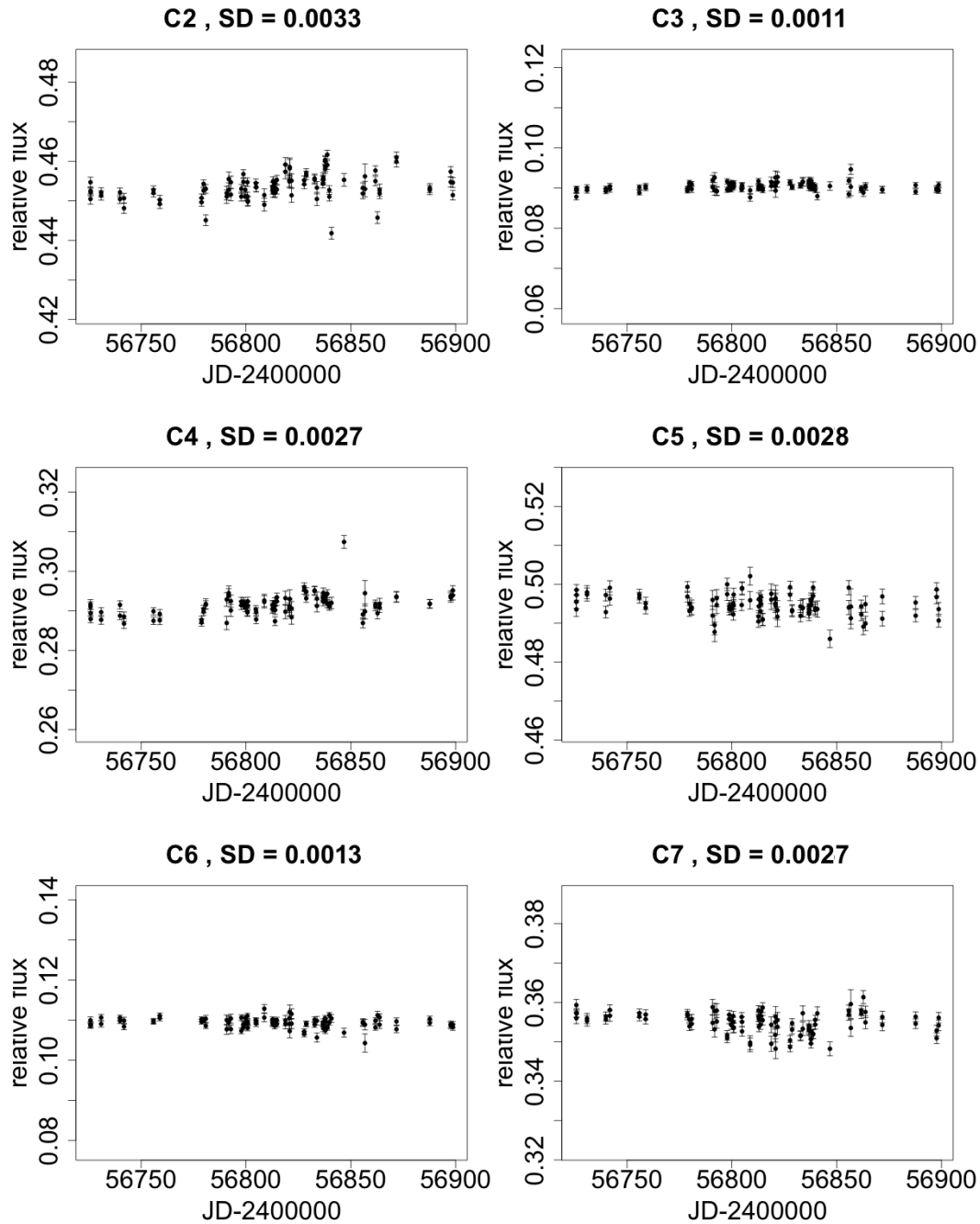


Figure 2.7 Comparison star light curves from the Strömgren y filter to check for significant variability. The label SD at the top of each plot indicates the standard deviation. The light curve from T1 (the AGN) is shown in Fig. 3.3. As C2 had the greatest variability among the comparison stars, it was removed as a comparison star. All comparison star plots were adjusted to the same span of relative flux as was given by NGC 5548 (T1). The marked comparison stars are shown in Fig. 2.3.

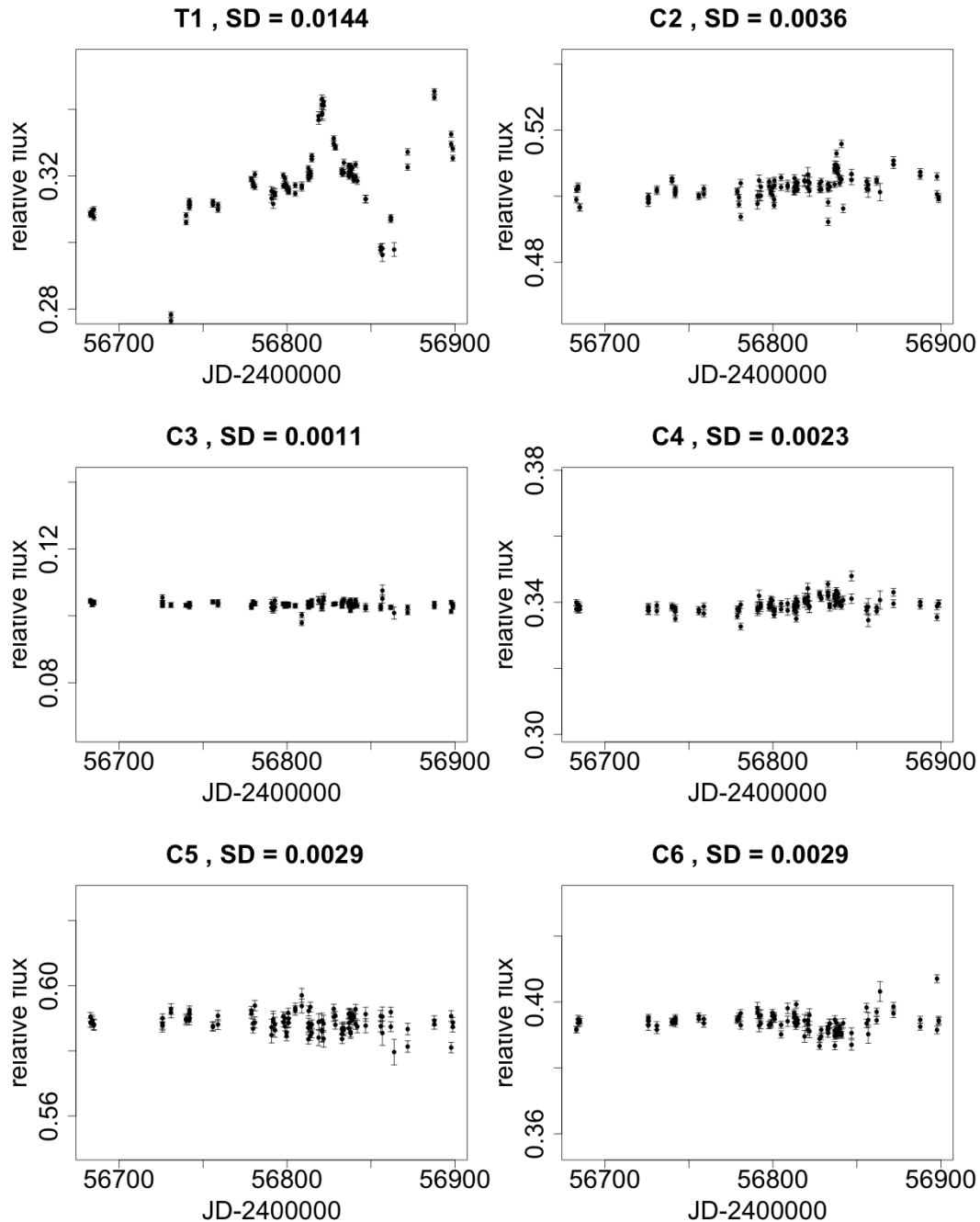


Figure 2.8 Comparison star light curves from the Johnson/Cousins V filter to check for significant variability. The label SD at the top of each plot indicates the standard deviation. T1 is the AGN. As C2 had the greatest variability among the comparison stars, it was removed as a comparison star. All comparison star plots were adjusted to the same span of relative flux as was given by NGC 5548 (T1). The marked comparison stars are shown in Fig. 2.4.

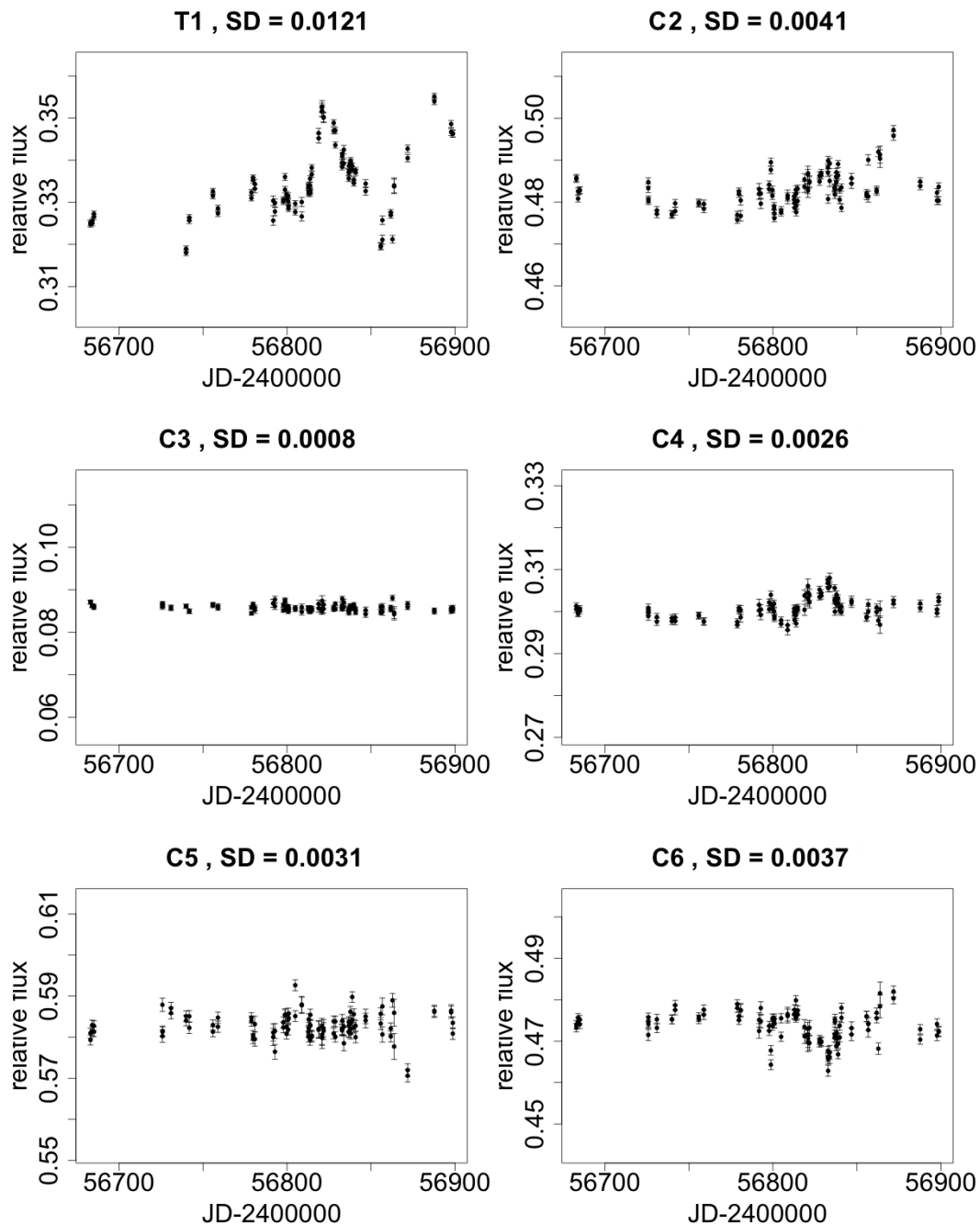


Figure 2.9 Comparison star light curves from the Johnson/Cousins R filter to check for significant variability. The label SD at the top of each plot indicates the standard deviation. T1 is the AGN. C2 was quite variable and thus removed as a comparison star. All comparison star plots were adjusted to the same span of relative flux as was given by NGC 5548 (T1). The marked comparison stars are shown in Fig. 2.5.

nulus=25, and outer radius of background annulus=30. These values were determined to be the best after several photometry runs with various parameters. Based on the aperture measurements from the variable aperture photometry we performed, our resulting light curves were found to be quite reasonable. The results from the variable aperture photometry proved to be inconsistent and unreliable, although helpful for determining the FWHM measurements to assess the best fixed aperture parameters for the given images. We took data from January 25 to August 29, 2014. For the $H\alpha_{10}$ filter, there were 88 frames from 39 nights after subtracting two frames because of bad seeing conditions, 99 data points from 43 nights for the Strömberg y filter, 106 points of good data for the Johnson/Cousins V filter from 46 nights and 104 data points in the Johnson/Cousins R filter from 45 nights. The photometric data are given for each filter in Appendix A.

2.5 Cross-correlation Analysis

The analysis to determine the time lags from the different light curves can be complex and has been developed in several studies (Chelouche & Daniel 2012; Chelouche et al. 2012; Edri et al. 2012; Haas et al. 2011; Nuñez et al. 2012). Further efforts have since advanced techniques for time lag analysis with photometric methods (Foreman-Mackey et al. 2013; Zu et al. 2013a;b; 2011). Cross-correlation analysis is straightforward when working with smooth, continuous data; however, as is standard with real data, the data used for our cross-correlation analysis are discrete points, with associated measurement errors and gaps due to unfavorable weather conditions that complicate the analysis.

When dealing with multiple time series analysis, cross-correlation is the best tool for seeking a time lag. Cross-correlation essentially compares several shifts of one data signal with another data signal until an optimal shift is found to align both signals. For example, a cross-correlation between $\sin(x)$ and $\cos(x)$ would produce $\pi/2$. In our case, the data signals are light curves from

light coming from the BLR. We compare $H\alpha$ light curves with continuum light curves to find the time lag between the two signals. The cross-correlation analysis tool is available in codes such as R or Matlab but only performs integer shifts. Because the shifts are measured in days, such analyses, although widely available, will only confirm the most likely time lags for shifts at an integer difference from the initial data point. This presents a lack of accuracy as further addressed below. Though it may seem an obvious solution to simply scale the time data, this requires data points to be inserted in place of gaps in the data. This in turn requires a modeling of the data, which can be much more complicated than simple linear regression. This is generally the approach taken in JAVELIN, which is explained further below.

The basis of cross-correlation analysis is the convolution of two complex functions $f(t)$ and $g(t)$. The cross-correlation is defined by

$$f \star g \equiv \bar{f}(-t) * g(t),$$

where $f * g$ is the convolution of $f(t)$ and $g(t)$ defined by

$$f * g = \int_{-\infty}^{\infty} f(\tau)g(t - \tau)d\tau.$$

Combining these two definitions, it follows that

$$[f \star g](t) = \int_{-\infty}^{\infty} f(-\tau)g(t - \tau)d\tau = \int_{-\infty}^{\infty} f(\tau)g(t + \tau)d\tau.$$

Cross-correlation analysis is therefore similar to a convolution, but with the intent of obtaining a time lag difference between two signals (Bracewell 1965; Papoulis 1962). In our case, f can represent the continuum filter data and g can represent the $H\alpha$ filter data.

The discrete cross-correlation function is the most accurate approach to determining the time lag. This is a method for measuring correlation functions without interpolating in the temporal domain (Edelson & Krolik 1988), which is essential when dealing with real, discrete data. Other methods in R and Matlab work best with non-discrete signals. We analyzed the cross-correlation of combinations of the two continuum filters with R, Matlab and a python script JAVELIN.

JAVELIN (*Just Another Vehicle for Estimating Lags In Nuclei*) can be used to model quasar variability with a variety of covariance functions (Zu et al. 2013b) and measure emission line time lags with spectroscopic (Zu et al. 2011) or photometric data (Zu et al. 2013a). We focused exclusively on its photometric capabilities for this project, which rely heavily on the quasar modeling with different covariance functions. In the models used for reverberation mapping, it is assumed that quasar variability can be described by a Damped Random Walk (DRW) model and that the emission line light curves are more or less identical to the continuum light curve, only delayed, smoothed, and possibly scaled. The DRW motion is modeled with the covariance function

$$S_{\text{DRW}}(\Delta t) = \sigma^2 \exp\left(-\left|\frac{\Delta t}{\tau_r}\right|\right),$$

where σ is the variability amplitude for timescales much less than τ_r and τ_r is the “relaxation time” needed for the variability to become uncorrelated (Kelly et al. 2009).

Traditional cross-correlation analysis techniques such as R and Matlab only sample integer shifts for similarity between light curves, which raises issues with determining lags. If a lag of 2.5 days is best, but a lag of 2 days or 3 days does not produce a very good fit, this lag will be missed entirely. JAVELIN first makes a continuum light curve model to determine the DRW parameters of the continuum light curve, introducing a non-discrete parameter to the mix, allowing more precise time lag determination. This makes the cross-correlation analysis from JAVELIN better than other methods for photometric reverberation mapping.

JAVELIN implements an affine-invariant ensemble sampler for Markov chain Monte Carlo (MCMC) called emcee (Foreman-Mackey et al. 2013). The code releases walkers from every point in space, which then collaboratively sample the posterior probability distributions. JAVELIN then tries to interpolate the continuum light curve based on the posteriors derived, and then shifts, smooths, and scales each continuum light curve to compare to the observed emission light curve. After doing this many times in a MCMC run, JAVELIN finally derives the posterior distribution of the lag t , the width of the top hat filter w , and the scale factor s of the $H\alpha$ data, along with

updated posteriors for the timescale τ and the amplitude σ of the continuum.

2.6 Obtaining Archival Velocity Dispersion

Much of the efficiency of this method is due to the use of archival spectral data to obtain the velocity dispersion for an AGN. This is approached with caution, as the dynamical time scale for the BLR gas, τ_{dyn} , is $\propto r/\Delta V$, which for typical luminous Seyferts is of order 3 – 5 years. Reverberation mapping experiments must be kept short relative to the dynamical timescale to avoid smearing the light travel-time effects (Peterson & Horne 2004), so recent velocity dispersions are required for results to be plausible for given photometric data. Although the most recent data would be ideal, we expect the relations between the BLR radius and the luminosity of the AGN would remain consistent enough to allow archival spectral data to be used within 5 – 10 years of the photometric results.

Fortunately, NGC 5548 may be one of the most studied active galaxies with reverberation mapping and has optical spectroscopy dating as far back as the early 1970s (Sergeev et al. 2007). This extensive data set includes a few long-term observing campaigns (Bentz et al. 2010; Park et al. 2012; Shapovalova et al. 2009). Shapovalova et al. (2009) performed a spectral monitoring program for NGC 5548 from 1996-2002, investigating the $H\beta$ and $H\alpha$ emission lines. The $H\alpha$ broad line profile has varied over time. In 1996, the red peak became brighter, while from 1998-2002 the blue peak became brighter.

Unfortunately, the majority of programs focusing on NGC 5548 did not observe the $H\alpha$ emission line, although recent campaigns have provided useful data on the $H\beta$ emission line. Bentz et al. (2007) reported a time lag of $\tau_{H\beta} = 6.3^{+2.6}_{-2.3}$ days (with $f = 5.5$), $\sigma_{line} = 2662 \pm 532$ km/s from the mean spectrum and $M_{BH} = 6.54 \times 10^7 M_{\odot}$. Just a few years later, Bentz et al. (2009b) refined this estimate to $\tau_{cent} = 4.24^{+0.91}_{-1.35}$ days for the centroid time lag estimate from

$H\beta$ vs. the Johnson/Cousins V band, $\sigma_{line} = 4266 \pm 65$ km/s from the mean spectrum and $M_{BH} = 14.9_{-5.1}^{+3.7} \times 10^6 M_{\odot}$ for $f = 1$ and $M_{BH} = 82_{-28}^{+20} \times 10^6 M_{\odot}$ for $f = 5.5$ (see Section 1.6 for discussion on the value of f). Park et al. (2012) reported the NGC 5548 mean spectra at $H\beta$ to have $\sigma_{mean} = 4354 \pm 25$ km/s. Another recent study using dynamical modeling with data from the 2008 Lick AGN Monitoring project gave $32.36_{-1.38}^{+1.70} M_{\odot}$ with a value for f that is specific to NGC 5548, $f = 2.63_{-1.38}^{+1.70}$ (Pancoast et al. 2014).

With so many variations of f , σ and the dynamical nature of the BLR, an argument for a full-fledged reverberation mapping campaign might be persuasive. However, given recent spectral information and reliable photometric observations of a given AGN, a black hole mass measurement based on reverberation mapping with cross-correlation should be reasonably accurate given the dynamical time scale mentioned above. We adopt the velocity dispersion of $\sigma_{mean} = 4354 \pm 25$ km/s from Park et al. (2012) and $f = 5.5$ for the results presented in Chapter 3.

Chapter 3

Results and Discussion

3.1 Review of Goal

The original intent of our project was to determine if cross-correlation could yield a reasonable time lag from photometric data in the $H\alpha_{10}$, Strömgen y , and Johnson/Cousins V and R filters to generate accurate estimates of SMBH mass for all eleven AGN listed in Table 3.1. The project was originally intended for a complete PhD dissertation and was later modified to a MS project. Our revised goal is to develop and apply this method to estimate the mass of the BH in NGC 5548 so it can be applied to other AGN by future students.

3.2 Data Acquisition

We began in 2012 with Mrk 926, for one quick observing season to complete an undergraduate senior thesis project. We then designated 10 additional AGN to investigate the feasibility of photometric reverberation mapping with meter-class telescopes as an expanded graduate-level project. Observations of Mrk 926 with the BVRI Johnson/Cousins filter set (see Table 2.1) are shown in Fig. 3.1. Although Mrk 926 proved to be an excellent candidate for reverberation mapping prior to

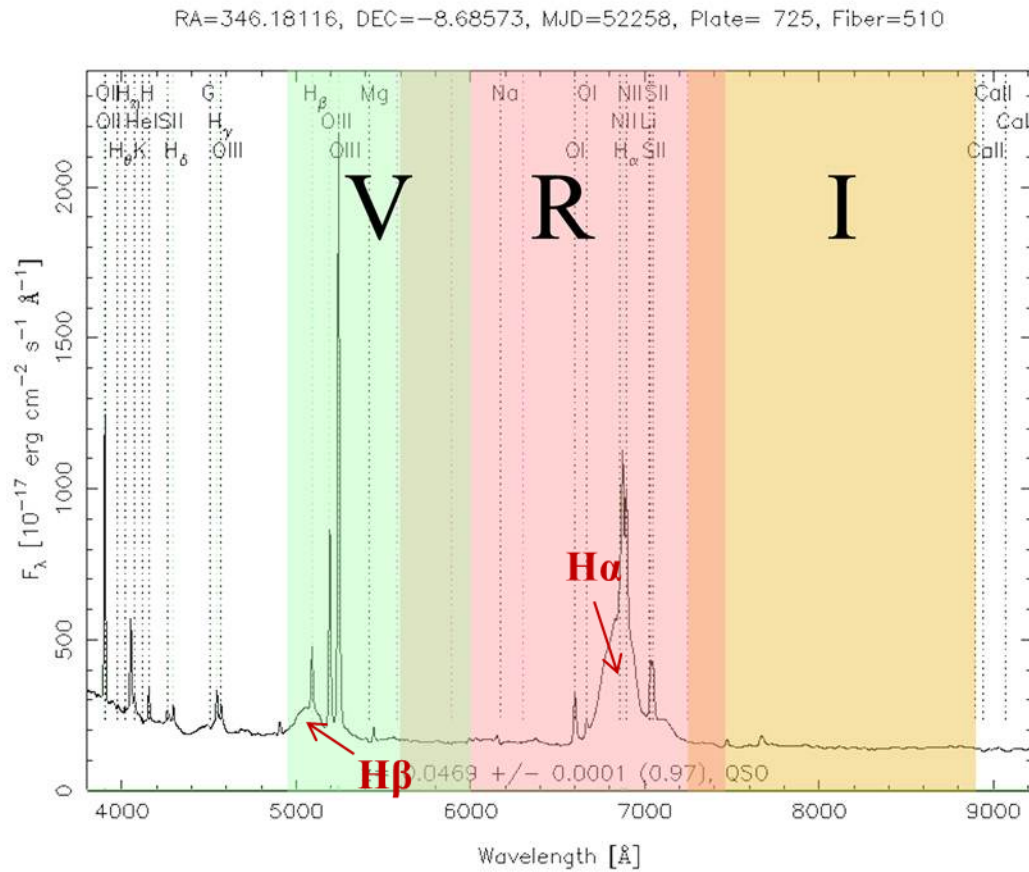


Figure 3.1 WMO broadband filter wavelength intervals overlaid on Sloan Digital Sky Survey (SDSS) spectra of galaxy Mrk 926. Wider filters ($\sim 1000\text{\AA}$) such as these have not been used in reverberation mapping prior to 2012. The filters are V (green), R (red), and I (yellow). The x -axis is the wavelength in \AA and the y -axis is the flux, F_λ .

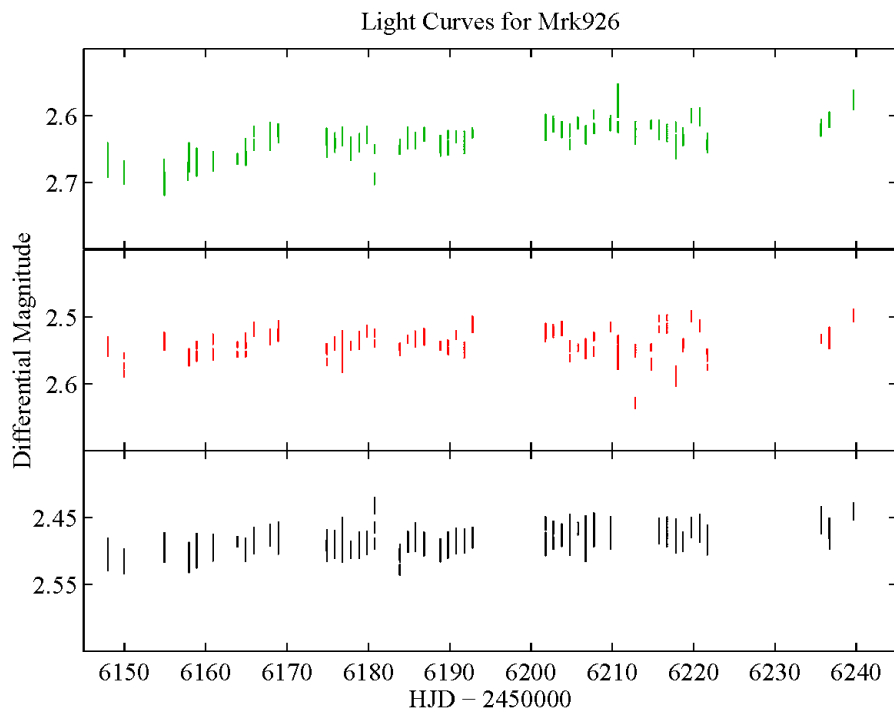


Figure 3.2 Mrk 926 light curves from WMO broadband filters V (top, green), R (middle, red) and I (bottom, black). The x -axis is the Julian Date (in days). The y -axis is the differential magnitude (mag) of Mrk 926 compared to several nonvariable stars around it. We expected significant variability in Mrk 926, but found less than 0.1 mag variability in each filter.

Table 3.1 Original AGN targets sorted by right ascension. In the original PhD project, we planned to obtain black hole mass estimates for at least four AGN and perhaps for all the AGN listed. We chose to focus on NGC 5548 as it is likely the best studied AGN by reverberation mapping (Sergeev et al. 2007) and was the subject of recent in-depth analysis by the Space Telescope and Optical Reverberation Mapping (STORM) Project (Edelson et al. 2015; Rosa et al. 2015).

Name	RA	Dec	z
UGC 3374	05 54 53.589	+46 26 21.76	0.02004
NGC 3227	10 23 30.57	+19 51 54.3	0.00365
NGC 4051	12 03 09.686	+44 31 52.54	0.00216
NGC 4151	12 10 32.574	+39 24 20.88	0.003262
Mrk 50	12 23 24.1414	+02 40 44.401	0.02386
NGC 4593	12 39 39.492	-05 20 39.16	0.008344
NGC 5548	14 17 59.513	+25 08 12.45	0.01627
Mrk 817	14 36 22.134	+58 47 38.93	0.031158
KIC 11178007	18 58 01.111	+48 50 23.40	0.079
Zw 229-015	19 05 25.928	+42 27 39.84	0.027532
Mrk 926	23 04 43.4911	-08 41 08.538	0.04702

our observing run (Kollatschny & Zetzl 2010), we found it to be relatively quiescent (see Fig. 3.2) and decided to pursue a cross-correlation analysis with a different candidate. Keeping Mrk 926 as a target, we added five more AGN to the 2013 observing season: KA 1858, Mrk 50, Mrk 817, NGC 4051 and Zw 229+015. In the following season we added the remaining AGN to the target list and observed all of them. The set of redshifted $H\alpha$ intermediate-band filters in Table 2.2 was acquired for a more accurate measurement of the broad-line emission feature. The original targets are given in Table 3.1. In the original PhD project, we planned to obtain black hole mass estimates for at least four AGN and perhaps for all the AGN listed. We chose to focus on NGC 5548 as it is likely the best studied AGN by reverberation mapping (Sergeev et al. 2007) and was the subject of recent in-depth analysis by the Space Telescope and Optical Reverberation Mapping (STORM) Project (Edelson et al. 2015; Rosa et al. 2015). When the project was changed to a masters thesis after the 2014 observing season, we decided to only fully analyze NGC 5548.

3.3 Analysis

Pairs of light curves for NGC 5548 are shown in Figs. 3.3, 3.4 and 3.5. These plots compare the relative flux in the Strömrgren y against the $H\alpha_{10}$ filter, the Johnson/Cousins V filter against the $H\alpha_{10}$ filter, and the Johnson/Cousins R filter against the $H\alpha_{10}$ filter. We did not find reliable time lags using the packages `xcorr` in Matlab and `ccf` in R (see Figs. 3.6 and 3.7). However, JAVELIN produced a time lag of $\tau_y = 3.3 \pm 0.1$ days comparing the Strömrgren y to the $H\alpha_{10}$, $\tau_V = 3.4 \pm 0.3$ days comparing Johnson/Cousins V to the $H\alpha_{10}$ and $\tau_R = 3.4 \pm 0.2$ days comparing Johnson/Cousins R to the $H\alpha_{10}$ (see Fig. 3.8 for one example). We ran the JAVELIN analysis 30 times for each filter to give statistically significant results. All three of our time lags are statistically indistinguishable from each other. Given that Bentz et al. (2009b) found a time lag of 4.25 days between an $H\beta$ emission and the Johnson/Cousins V filter, these results are reasonable.

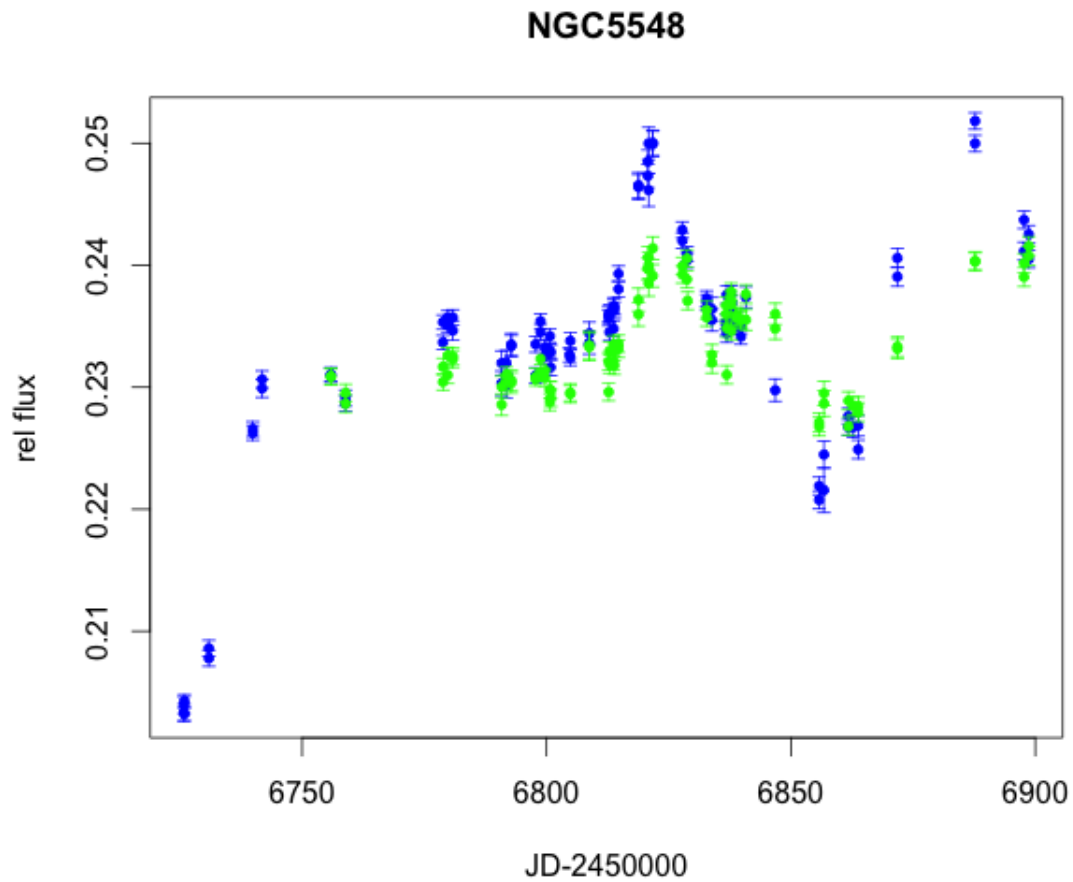


Figure 3.3 NGC 5548 Light Curve Comparison between Strömgren y (blue) and $H\alpha_{10}$ (green). This plot shows relative flux on the y -axis and in both plots the $H\alpha_{10}$ flux data was shifted by a small amount to enable data from all filters to align along the y -axis. Data for all light curves can be found in Appendix A.

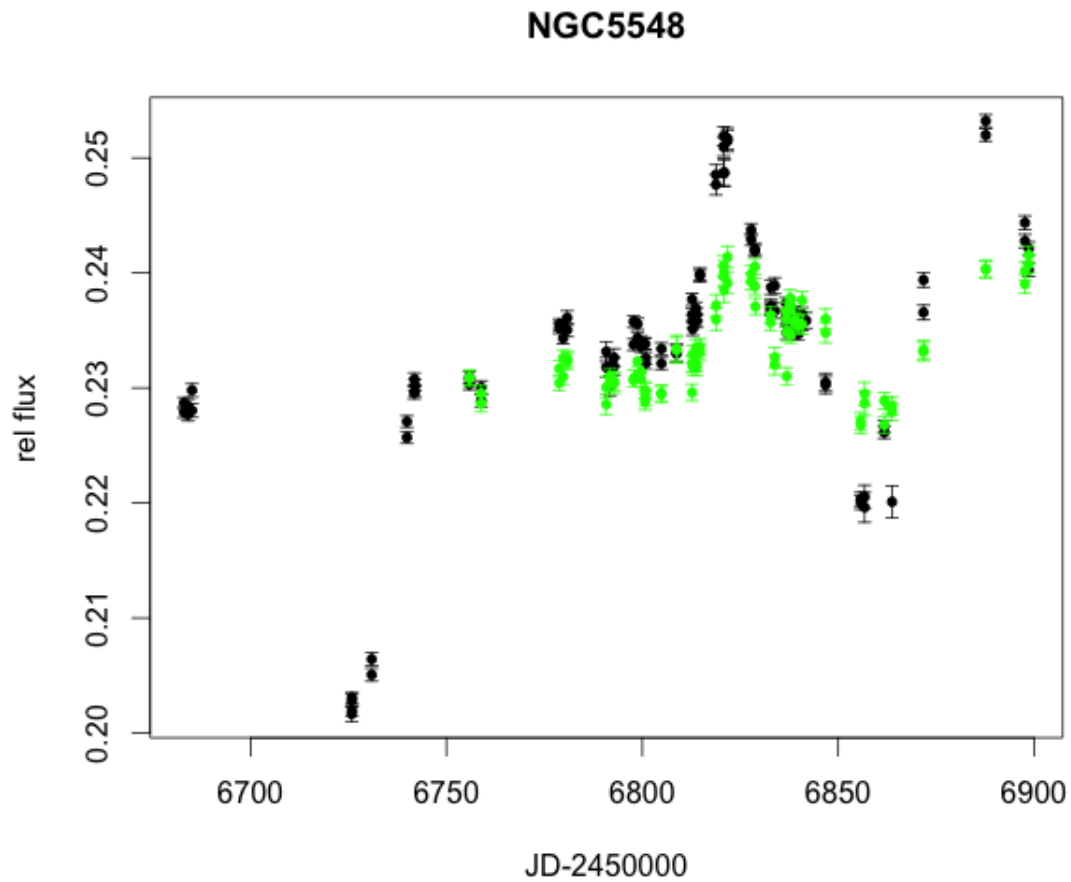


Figure 3.4 NGC 5548 Light Curve Comparison between Johnson/Cousins V filter (black) and $H\alpha_{10}$ (green). This plot shows relative flux on the y-axis and in both plots the $H\alpha_{10}$ flux data was shifted by a small amount to enable data from all filters to align along the y-axis. Data for all light curves can be found in Appendix A.

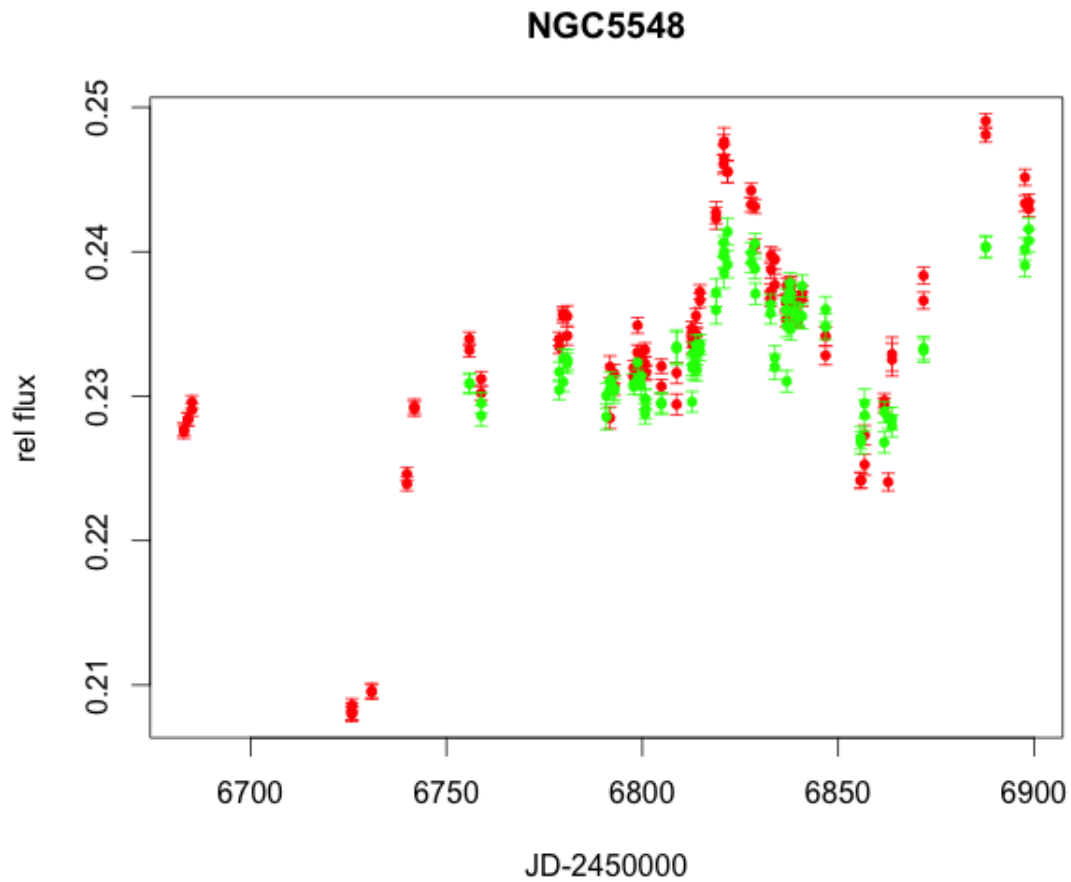


Figure 3.5 NGC 5548 Light Curve Comparison between Johnson/Cousins R filter (red) and H α_{10} (green). This plot shows relative flux on the y-axis and in both plots the H α_{10} flux data was shifted by a small amount to enable data from all filters to align along the y-axis. Data for all light curves can be found in Appendix A.

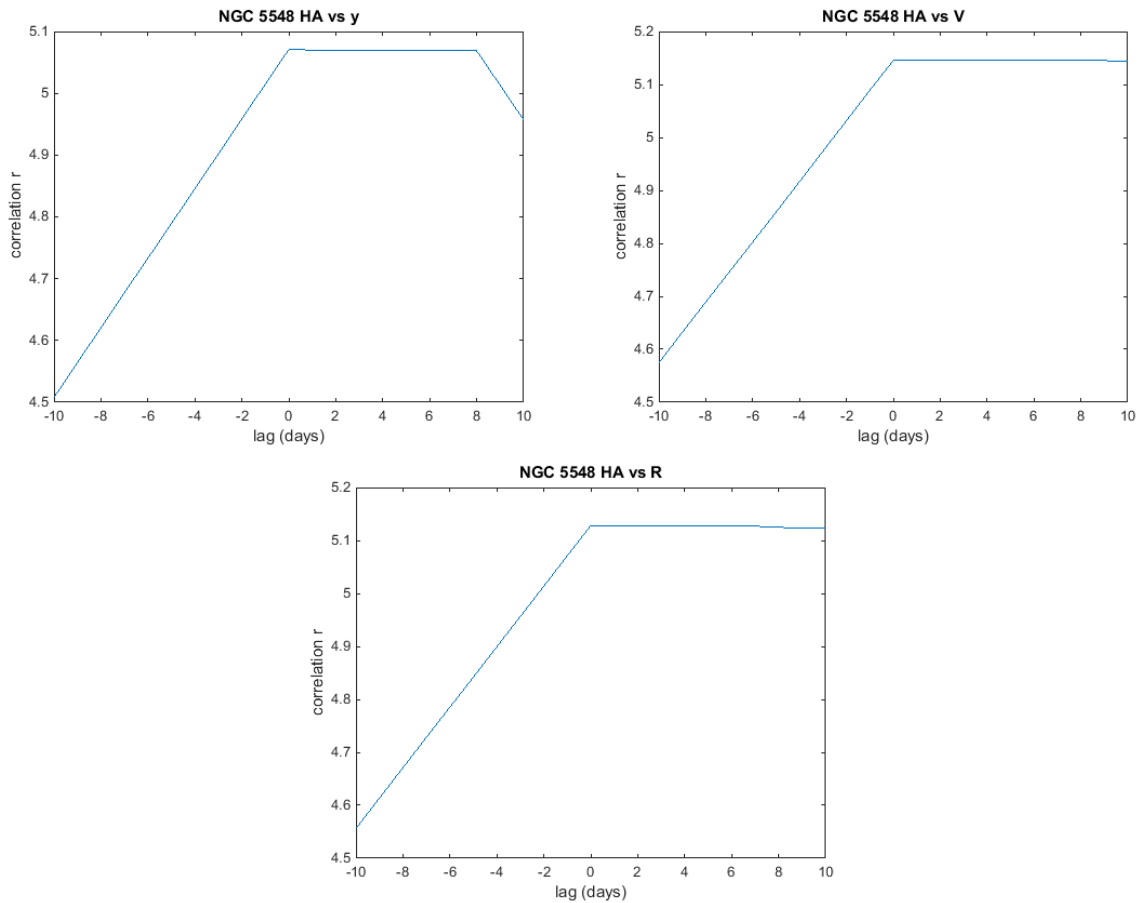


Figure 3.6 Top left image: Matlab cross-correlation analysis of the Strömgen y and $H\alpha_{10}$ filters, indicating a maximum likely lag of 0 days. Top right image: Matlab cross-correlation analysis of the Johnson/Cousins V and $H\alpha_{10}$ filters, giving a maximum likely lag of 2 days. Bottom image: Matlab cross-correlation analysis of the Johnson/Cousins R and $H\alpha_{10}$ filters, giving a maximum likely lag of 0 days. This analysis supports the need for CCF analysis using JAVELIN to determine time lags with more precision than integer days. Though these graphs look nearly identical, the Matlab cross-correlation analysis reported slightly different maximum lags. This only further emphasizes the unreliability of this method.

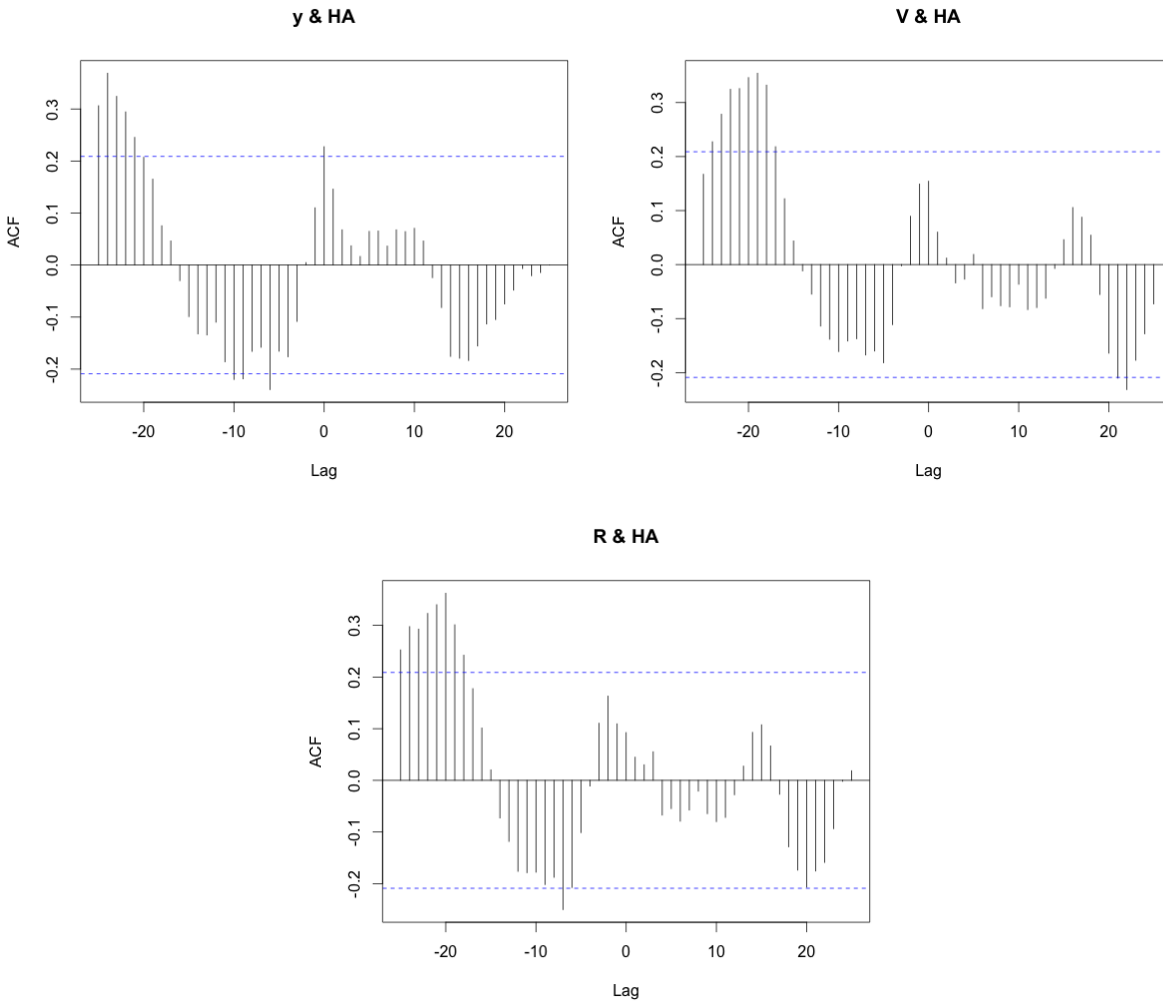


Figure 3.7 Top left image: R CCF analysis of the Strömgren y and $H\alpha_{10}$ filters, giving a maximum likely lag of -24 days. Top right image: R CCF analysis of the Johnson/Cousins V and $H\alpha_{10}$ filters, giving a maximum likely lag of -19 days. Bottom image: R CCF analysis of the Johnson/Cousins R and $H\alpha_{10}$ filters, giving a maximum likely lag of -20 days. This analysis supports the need for CCF analysis using JAVELIN to determine time lags with more precision than integer days.

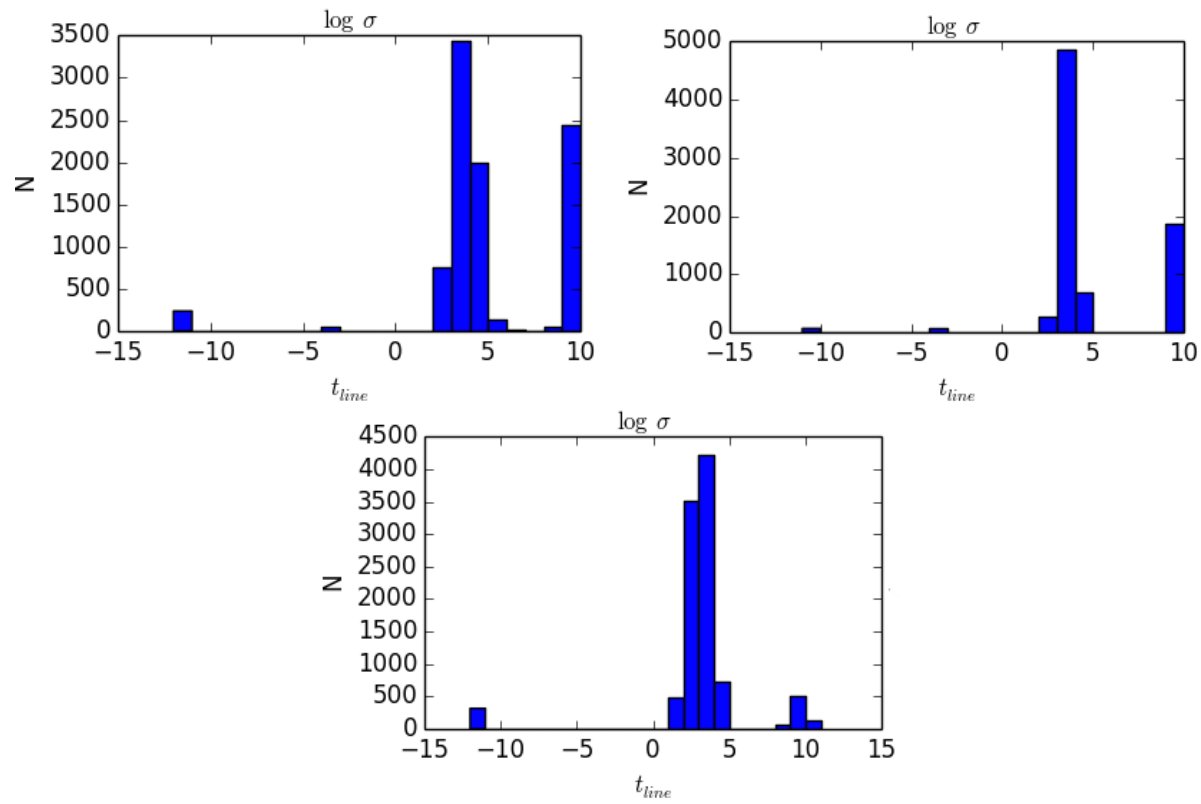


Figure 3.8 We ran the JAVELIN analysis 30 times for each filter to obtain reasonable statistics. Shown here are examples of a single JAVELIN analysis for each filter. Top left image: JAVELIN analysis comparing Strömgren y band with $H\alpha_{10}$. With a lag limit set to ± 20 days, this run produced a lag of 3.2 days. Top right image: JAVELIN analysis comparing Johnson/Cousins V band with $H\alpha_{10}$. With a lag limit set to ± 20 days, this run produced a lag of 3.3 days. Bottom image: JAVELIN analysis comparing Johnson/Cousins R band with $H\alpha_{10}$. With a lag limit set to ± 20 days, this run produced a lag of 3.4 days.

The variety of choices of $\Delta\nu$ and f can lead to a range of black hole masses, even with only one time lag τ . Using the time lag from the Strömgren y and $H\alpha_{10}$ filters and a velocity dispersion of 4354 ± 25 km/s (Park et al. 2012), we estimate the virial mass of the SMBH to be $M_{\text{BH}} = 12.2 \pm 0.4 \times 10^6 M_{\odot}$ (with $f = 1$). The Strömgren y filter gave the best wavelength range and position to provide a continuum free of significant emission features (see Fig. 2.1). We chose the velocity dispersion from Park et al. (2012) because it is a recent and reliable measurement from a large collaboration. With $f = 2.63^{+1.70}_{-1.38}$ from Park et al. (2012), we estimate a SMBH mass of $M_{\text{BH}} = 32.1 \pm 1.1 \times 10^6 M_{\odot}$. Park et al. (2012) exclusively investigated NGC 5548 to determine what may be the best f value based on the nature of the gas, inclination angle, etc. Woo et al. (2010) studied 24 AGN that had been recently reverberation mapped and found that the general consensus for the best value of f using the quiescent $M_{\text{BH}} - \sigma^*$ relation determined by Gültekin et al. (2009) was $f = 5.248$, yielding a SMBH mass of $M_{\text{BH}} = 64.1 \pm 2.1 \times 10^6 M_{\odot}$ for our data. In recent literature (Bentz et al. 2009b; Denney et al. 2010; Pancoast et al. 2014), black hole mass estimates were given with $f = 5.5$. With this value, our black hole mass estimate is $M_{\text{BH}} = 67.2 \pm 2.2 \times 10^6 M_{\odot}$. Since $f = 5.5$ is the most commonly accepted value in the literature, we adopt it for our estimate of the SMBH mass.

These masses agree well with published data. The most recent, best mass estimates for NGC 5548 (according to Edelson et al. 2015) are from Pancoast et al. (2014), and Denney et al. (2010). Pancoast et al. (2014) report a black hole mass estimate of $\log M_{\text{BH}} = 7.59^{+0.24}_{-0.21}$, or $M_{\text{BH}} = 38.91^{+1.74}_{-1.62} \times 10^6 M_{\odot}$ and Denney et al. (2010) produced an estimate $M_{\text{BH}} = 44.2^{+9.9}_{-13.8} \times 10^6 M_{\odot}$. Bentz et al. (2009b) found $M_{\text{BH}} = 82^{+20}_{-28} M_{\odot}$. In comparison with these recent mass estimates for NGC 5548, our $M_{\text{BH}} = 67.2 \pm 2.2 \times 10^6 M_{\odot}$ is reasonable, and a good indication that this method of photometric reverberation mapping should be pursued.

3.4 Calculations

As discussed in Section 1.4, M_{BH} can be obtained from reverberation mapping by

$$M_{\text{BH}} = f \frac{\Delta v^2 c \tau}{G},$$

where f is a scaling factor, Δv is the Doppler broadening velocity, $c\tau$ is the radius of the BLR and G is the gravitational constant. In our final calculation we used $f = 5.5$, $\Delta v = 4354 \pm 25$ km/s (Park et al. 2012) and $\tau = 3.3 \pm 0.1$. We calculated the mass by putting all values into SI units and then converting to solar masses as follows:

$$M_{\text{BH}} = (5.5) \frac{(4354 \pm 25 \times 10^3 \text{ m s}^{-1})^2 (3 \times 10^8 \text{ m s}^{-1}) (3.3 \pm 0.1 \text{ days}) (86400 \text{ s day}^{-1})}{6.67384 \times 10^{-11} \text{ m}^3 \text{ kg}^{-1} \text{ s}^{-2}}.$$

This gives an answer in kilograms, which can be divided by $1.9891 \times 10^{30} \text{ kg } M_{\odot}^{-1}$ to obtain $M_{\text{BH}} = 67.2 \pm 2.2 \times 10^6 M_{\odot}$.

Errors were calculated according to the propagation of error. In this method, the final error from any equation h can be found from

$$s_h = \sqrt{\left(\frac{\partial h}{\partial x}\right)^2 s_x^2 + \left(\frac{\partial h}{\partial y}\right)^2 s_y^2 + \left(\frac{\partial h}{\partial z}\right)^2 s_z^2 + \dots}$$

Applying this to our mass estimate, we find

$$s_M = \sqrt{\left(f \frac{\Delta v^2 c}{G}\right)^2 s_{\tau}^2 + \left(f \frac{2\Delta v c \tau}{G}\right)^2 s_{\Delta v}^2 + \left(\frac{\Delta v^2 c \tau}{G}\right)^2 s_f^2.}$$

3.5 Further Work

Though we have obtained reasonable results for the time lag for NGC 5548, analysis of Mrk 817, NGC 4051, NGC 4151 and Zw 229, further analysis with JAVELIN should be performed in the future. This project is ready and available for students to thoroughly investigate the feasibility of our photometric reverberation mapping technique with several AGN. The other AGN in Table 3.1

are yet to be fully analyzed, and not enough $H\alpha$ data for some of them were obtained in the 2014 observing season (e.g., KA 1858) for cross-correlation analysis to be done. A more refined cross-correlation analysis is needed to fully evaluate the feasibility of photometric reverberation mapping with meter-class telescopes. Such an analysis would need to sample time lags at intervals shorter than integer days, which is what is currently available in Matlab and R. JAVELIN has proved to be a great resource for many groups so far, but needs to be further tested with additional data sets to validate its use with WMO data. WMO data is a good representation of what is possible and usually available at other small observatories. Also, images have already been captured from the 2014 observing season and are available for analysis. We hope that this project will continue to be advanced so that reverberation mapping can become a widely available method for use at other small observatories.

Appendix A

Data Tables

Table A.1 Photometry results from the $H\alpha_{10}$ filter. The relative flux is in arbitrary flux units. Comparison light curves are shown in Figs. 3.3, 3.4 and 3.5.

J.D.–2456000	AGN Rel. Flux	Error	J.D.–2456000	AGN Rel. Flux	Error
755.8909	0.2308	0.0007	791.7812	0.2311	0.0006
755.8924	0.2309	0.0007	791.7841	0.2304	0.0006
758.8933	0.2295	0.0007	792.8075	0.2304	0.0008
758.8948	0.2287	0.0007	792.8090	0.2306	0.0008
778.8175	0.2317	0.0007	797.7885	0.2308	0.0007
778.8190	0.2304	0.0007	797.7900	0.2307	0.0000
779.7962	0.2310	0.0007	798.7838	0.2312	0.0007
779.7977	0.2326	0.0007	798.7853	0.2323	0.0000
780.8443	0.2323	0.0007	799.6928	0.2308	0.0007
780.8458	0.2325	0.0007	799.6943	0.2314	0.0000
790.8284	0.2300	0.0009	800.6949	0.2288	0.0007
790.8299	0.2286	0.0009	800.6964	0.2298	0.0007

J.D.–2456000	AGN Rel. Flux	Error	J.D.–2456000	AGN Rel. Flux	Error
800.8515	0.2298	0.0007	821.7434	0.2414	0.0009
800.8530	0.2291	0.0007	827.7822	0.2392	0.0007
804.8662	0.2296	0.0007	827.7837	0.2399	0.0007
804.8677	0.2294	0.0007	828.7476	0.2406	0.0007
808.7557	0.2333	0.0011	828.7492	0.2388	0.0007
808.7572	0.2334	0.0011	828.8524	0.2371	0.0007
812.7188	0.2296	0.0007	832.7472	0.2363	0.0007
812.7203	0.2321	0.0007	832.7487	0.2357	0.0007
812.8777	0.2330	0.0007	833.8317	0.2320	0.0009
812.8792	0.2319	0.0007	833.8332	0.2326	0.0009
813.7198	0.2321	0.0007	836.7582	0.2360	0.0007
813.7213	0.2335	0.0007	836.7598	0.2367	0.0007
813.8600	0.2318	0.0007	836.8598	0.2310	0.0007
813.8615	0.2329	0.0007	836.8614	0.2348	0.0008
814.7268	0.2336	0.0007	837.7415	0.2378	0.0007
814.7283	0.2332	0.0007	837.7430	0.2372	0.0007
818.8176	0.2372	0.0010	837.8353	0.2368	0.0007
818.8192	0.2360	0.0010	837.8368	0.2346	0.0007
820.7494	0.2406	0.0009	838.7809	0.2357	0.0007
820.7509	0.2397	0.0009	838.7824	0.2358	0.0007
820.8766	0.2385	0.0011	839.7620	0.2355	0.0007
820.8781	0.2400	0.0011	839.7635	0.2356	0.0007
821.7419	0.2391	0.0009	840.7891	0.2376	0.0008

J.D.-2456000	AGN Rel. Flux	Error
840.7906	0.2355	0.0009
846.7935	0.2348	0.0009
846.7950	0.2360	0.0009
855.7711	0.2268	0.0008
855.7726	0.2271	0.0008
856.7585	0.2295	0.0010
856.7600	0.2287	0.0011
861.7497	0.2268	0.0007
861.7512	0.2289	0.0007
862.7557	0.2285	0.0007
863.7525	0.2279	0.0008
863.7540	0.2284	0.0008
871.7756	0.2332	0.0008
871.7771	0.2333	0.0008
887.6773	0.2403	0.0007
887.6788	0.2404	0.0007
897.6760	0.2402	0.0008
897.6775	0.2390	0.0008
898.6595	0.2408	0.0008
898.6610	0.2416	0.0008

Table A.2 Photometry results from the Strömgen y filter. The relative flux is in arbitrary flux units. Comparison light curves are shown in Fig. 3.3.

J.D.–2456000	AGN Rel. Flux	Error	J.D.–2456000	AGN Rel. Flux	Error
725.8363	0.1695	0.0007	790.8257	0.1959	0.0010
725.8392	0.1689	0.0007	791.7750	0.1957	0.0010
725.9110	0.1688	0.0005	791.7779	0.1976	0.0010
725.9139	0.1698	0.0005	792.8013	0.1991	0.0009
730.9260	0.1742	0.0007	792.8042	0.1990	0.0009
730.9289	0.1734	0.0007	797.7827	0.1991	0.0006
739.9237	0.1921	0.0006	797.7856	0.1965	0.0006
739.9266	0.1918	0.0006	798.7766	0.2001	0.0006
741.8268	0.1955	0.0007	798.7810	0.2010	0.0006
741.8297	0.1962	0.0007	799.6871	0.1988	0.0006
755.8839	0.1966	0.0006	799.6900	0.1981	0.0006
755.8867	0.1966	0.0006	800.6890	0.1998	0.0006
758.8878	0.1942	0.0007	800.6919	0.1986	0.0006
758.8906	0.1947	0.0007	800.8557	0.1972	0.0007
778.8117	0.1993	0.0006	800.8586	0.1984	0.0006
778.8146	0.2009	0.0006	804.7121	0.1982	0.0006
779.7903	0.2006	0.0006	804.8705	0.1994	0.0007
779.7932	0.2013	0.0006	804.8734	0.1980	0.0007
780.8379	0.2002	0.0008	808.7497	0.1992	0.0009
780.8408	0.2013	0.0006	808.7526	0.2000	0.0009
790.8228	0.1975	0.0010	812.7132	0.2015	0.0006

J.D.–2456000	AGN Rel. Flux	Error	J.D.–2456000	AGN Rel. Flux	Error
812.7161	0.2013	0.0006	833.8262	0.2020	0.0010
812.8817	0.2017	0.0007	833.8291	0.2011	0.0009
812.8846	0.2001	0.0007	836.7524	0.2004	0.0006
813.7142	0.2004	0.0006	836.7552	0.2009	0.0006
813.7171	0.2022	0.0006	836.8642	0.2032	0.0007
813.8640	0.2019	0.0007	836.8671	0.2000	0.0007
813.8669	0.2022	0.0007	837.7352	0.2018	0.0006
814.7213	0.2049	0.0007	837.7381	0.2033	0.0006
814.7242	0.2036	0.0007	837.8394	0.2024	0.0007
818.8120	0.2121	0.0010	837.8423	0.2009	0.0007
818.8148	0.2120	0.0010	838.7751	0.2012	0.0006
820.7438	0.2129	0.0010	838.7780	0.2006	0.0006
820.7467	0.2141	0.0010	839.7564	0.1997	0.0006
820.8807	0.2156	0.0013	839.7593	0.2006	0.0006
820.8836	0.2117	0.0013	840.7862	0.2030	0.0009
821.7365	0.2155	0.0011	846.7906	0.1953	0.0009
821.7394	0.2156	0.0010	855.7655	0.1863	0.0007
827.7765	0.2085	0.0006	855.7684	0.1875	0.0007
827.7794	0.2076	0.0006	856.7530	0.1871	0.0018
828.7419	0.2065	0.0006	856.7559	0.1901	0.0011
828.7448	0.2060	0.0006	861.7443	0.1932	0.0006
832.7417	0.2028	0.0006	861.7472	0.1923	0.0006
832.7446	0.2025	0.0006	862.7523	0.1923	0.0009

J.D.–2456000	AGN Rel. Flux	Error
863.7471	0.1924	0.0008
863.7500	0.1905	0.0008
871.7699	0.2062	0.0008
871.7728	0.2046	0.0008
887.6717	0.2156	0.0007
887.6745	0.2174	0.0007
897.6704	0.2093	0.0007
897.6733	0.2067	0.0007
898.6538	0.2081	0.0007
898.6567	0.2061	0.0007

Table A.3 Photometry results from the Johnson/Cousins V filter. The relative flux is in arbitrary flux units. Comparison light curves are shown in Fig. 3.4.

J.D.–2456000	AGN Rel. Flux	Error	J.D.–2456000	AGN Rel. Flux	Error
683.0001	0.2191	0.0005	758.8854	0.2213	0.0006
683.0013	0.2199	0.0005	778.8081	0.2264	0.0005
684.0328	0.2189	0.0006	778.8092	0.2267	0.0005
684.0336	0.2196	0.0006	779.7849	0.2267	0.0005
685.0409	0.2192	0.0006	779.7861	0.2255	0.0005
685.0417	0.2210	0.0006	780.8339	0.2273	0.0006
725.8297	0.1928	0.0007	780.8351	0.2262	0.0006
725.8309	0.1940	0.0006	790.8189	0.2244	0.0009
725.9050	0.1931	0.0004	790.8201	0.2230	0.0009
725.9062	0.1943	0.0005	791.7712	0.2214	0.0009
730.9178	0.1976	0.0006	791.7724	0.2231	0.0009
730.9190	0.1963	0.0006	792.7976	0.2238	0.0008
739.9200	0.2169	0.0005	792.7988	0.2231	0.0008
739.9212	0.2183	0.0005	797.7790	0.2250	0.0005
741.8212	0.2220	0.0005	797.7802	0.2270	0.0005
741.8224	0.2208	0.0005	798.7711	0.2268	0.0005
741.9353	0.2215	0.0005	798.7723	0.2255	0.0005
741.9365	0.2209	0.0005	799.6834	0.2252	0.0005
755.8779	0.2221	0.0005	799.6845	0.2248	0.0005
755.8790	0.2215	0.0005	800.6854	0.2251	0.0005
758.8842	0.2201	0.0006	800.6866	0.2250	0.0005

J.D.–2456000	AGN Rel. Flux	Error	J.D.–2456000	AGN Rel. Flux	Error
800.8611	0.2234	0.0005	821.7341	0.2429	0.0009
800.8622	0.2238	0.0005	827.7729	0.2341	0.0005
804.8759	0.2233	0.0005	827.7741	0.2350	0.0005
804.8770	0.2246	0.0005	828.7382	0.2331	0.0005
808.7457	0.2242	0.0008	828.7393	0.2333	0.0005
808.7469	0.2242	0.0008	832.7363	0.2282	0.0005
812.7095	0.2289	0.0005	832.7375	0.2280	0.0005
812.7106	0.2276	0.0005	832.8536	0.2283	0.0006
812.8873	0.2270	0.0006	832.8547	0.2300	0.0006
812.8885	0.2263	0.0006	833.8210	0.2279	0.0007
813.7107	0.2271	0.0005	833.8222	0.2301	0.0007
813.7119	0.2281	0.0005	836.7469	0.2273	0.0005
813.8693	0.2270	0.0006	836.7480	0.2285	0.0005
813.8705	0.2276	0.0006	836.8712	0.2260	0.0006
814.7177	0.2311	0.0005	836.8724	0.2271	0.0006
814.7188	0.2309	0.0005	837.7297	0.2274	0.0005
818.8084	0.2397	0.0009	837.7309	0.2284	0.0005
818.8096	0.2389	0.0009	837.8463	0.2267	0.0006
820.7402	0.2422	0.0008	837.8475	0.2269	0.0006
820.7414	0.2431	0.0008	838.7714	0.2265	0.0005
820.8860	0.2399	0.0012	838.7725	0.2278	0.0005
820.8872	0.2400	0.0012	839.7529	0.2259	0.0005
821.7329	0.2427	0.0009	839.7541	0.2264	0.0005

J.D.–2456000	AGN Rel. Flux	Error
840.7774	0.2267	0.0005
840.7785	0.2276	0.0006
841.8290	0.2271	0.0007
846.7841	0.2215	0.0008
846.7852	0.2217	0.0008
855.7617	0.2112	0.0006
855.7629	0.2115	0.0006
856.7491	0.2117	0.0010
856.7503	0.2108	0.0013
861.7406	0.2179	0.0005
861.7418	0.2173	0.0005
863.7433	0.2113	0.0014
871.7662	0.2278	0.0006
871.7673	0.2306	0.0006
887.6668	0.2432	0.0006
887.6679	0.2444	0.0006
897.6669	0.2340	0.0006
897.6680	0.2356	0.0006
898.6500	0.2333	0.0006
898.6512	0.2315	0.0006
683.0035	0.2311	0.0005
683.0043	0.2313	0.0005

Table A.4 Photometry results from the Johnson/Cousins R filter. The relative flux is in arbitrary flux units. Comparison light curves are shown in Fig. 3.5.

J.D.–2456000	AGN Rel. Flux	Error	J.D.–2456000	AGN Rel. Flux	Error
684.0346	0.2320	0.0004	779.7880	0.2393	0.0005
684.0354	0.2320	0.0004	780.8318	0.2391	0.0007
685.0427	0.2332	0.0004	780.8326	0.2378	0.0006
685.0435	0.2326	0.0004	791.7693	0.2356	0.0008
725.8324	0.2116	0.0005	791.7701	0.2321	0.0007
725.8333	0.2118	0.0006	792.7951	0.2351	0.0007
725.9075	0.2116	0.0004	792.7959	0.2343	0.0007
725.9083	0.2122	0.0004	797.7771	0.2355	0.0005
730.9229	0.2131	0.0005	797.7779	0.2349	0.0000
730.9237	0.2132	0.0005	798.7734	0.2366	0.0005
739.9150	0.2282	0.0005	798.7742	0.2385	0.0005
739.9158	0.2275	0.0005	799.6812	0.2366	0.0005
741.8236	0.2329	0.0005	799.6820	0.2357	0.0005
741.8245	0.2327	0.0005	800.6834	0.2358	0.0005
755.8803	0.2375	0.0005	800.6842	0.2368	0.0005
755.8811	0.2368	0.0005	800.8635	0.2352	0.0005
758.8820	0.2338	0.0005	800.8643	0.2352	0.0005
758.8828	0.2348	0.0005	804.8782	0.2343	0.0005
778.8061	0.2375	0.0005	804.8790	0.2357	0.0005
778.8069	0.2370	0.0005	808.7435	0.2352	0.0007
779.7872	0.2391	0.0005	808.7443	0.2330	0.0007

J.D.–2456000	AGN Rel. Flux	Error	J.D.–2456000	AGN Rel. Flux	Error
812.7072	0.2379	0.0005	832.7395	0.2403	0.0005
812.7081	0.2383	0.0005	832.8561	0.2433	0.0006
812.8897	0.2371	0.0005	832.8569	0.2424	0.0006
812.8905	0.2375	0.0005	833.8233	0.2431	0.0007
813.7088	0.2391	0.0005	833.8241	0.2413	0.0008
813.7096	0.2378	0.0005	836.7493	0.2389	0.0005
813.8715	0.2373	0.0005	836.7501	0.2401	0.0005
813.8724	0.2378	0.0005	836.8693	0.2400	0.0005
814.7157	0.2402	0.0005	836.8701	0.2412	0.0005
814.7165	0.2408	0.0005	837.7320	0.2408	0.0005
818.8064	0.2459	0.0008	837.7328	0.2411	0.0005
818.8072	0.2463	0.0008	837.8444	0.2413	0.0005
820.7382	0.2510	0.0007	837.8452	0.2414	0.0005
820.7391	0.2496	0.0007	838.7692	0.2400	0.0005
820.8883	0.2500	0.0009	838.7700	0.2401	0.0005
820.8892	0.2512	0.0009	839.7511	0.2388	0.0005
821.7309	0.2491	0.0008	839.7519	0.2389	0.0005
821.7317	0.2491	0.0008	840.7796	0.2407	0.0005
827.7709	0.2478	0.0005	840.7804	0.2403	0.0005
827.7717	0.2468	0.0005	846.7821	0.2364	0.0006
828.7362	0.2440	0.0005	846.7829	0.2377	0.0006
828.7370	0.2467	0.0005	855.7597	0.2278	0.0005
832.7387	0.2408	0.0005	855.7605	0.2277	0.0005

J.D.–2456000	AGN Rel. Flux	Error
856.7471	0.2309	0.0007
856.7479	0.2288	0.0007
861.7387	0.2330	0.0005
861.7395	0.2333	0.0005
862.7438	0.2276	0.0006
863.7413	0.2365	0.0012
863.7421	0.2361	0.0011
871.7643	0.2402	0.0006
871.7651	0.2419	0.0006
887.6643	0.2526	0.0005
887.6651	0.2517	0.0005
897.6648	0.2487	0.0006
897.6656	0.2469	0.0006
898.6481	0.2466	0.0005
898.6490	0.2470	0.0005

Bibliography

Bentz, M. C., Denney, K. D., Cackett, E. M., et al. 2007, ApJ, 662, 205

Bentz, M. C., Peterson, B. M., Netzer, H., Pogge, R. W., & Vestergaard, M. 2009a, ApJ, 697, 160

Bentz, M. C., Walsh, J. L., Barth, A. J., et al. 2009b, ApJ, 705, 199

Bentz, M. C., Walsh, J. L., et al. 2010, ApJ, 716, 993

Bracewell, R. 1965, The Fourier Transform and Its Applications (Pentagram Notation for Cross Correlation: New York: McGraw-Hill)

Chelouche, D., & Daniel, E. 2012, ApJ, 747, 62

Chelouche, D., Daniel, E., & Kaspi, S. 2012, ApJ, 750, 43

Collins, K., & Kielkopf, J. 2013, ASCL, 1309, 1

Denney, K. D., Peterson, B. M., et al. 2010, ApJ, 721, 715

Edelson, R., et al. 2015, arXiv:astro-ph/1501.05951

Edelson, R. A., & Krolik, J. H. 1988, ApJ, 333, 646

Edri, H., et al. 2012, ApJ, 756, 73

Ferrarese, L., & Merritt, D. 2000, ApJ, 539, 9

- Foreman-Mackey, D., Hogg, D. W., Lang, D., & Goodman, J. 2013, arXiv:astro-ph/1202.3665v4
- Gebhardt, K., et al. 2000, ApJ, 539, 13
- Gültekin, K., et al. 2009, ApJ, 698, 198
- Haas, M., et al. 2011, ApJ, 535, 73
- Kelly, B. C., Bechtold, J., & Siemiginowska, A. 2009, ApJ, 698, 895
- Kollatschny, W., & Zetzl, M. 2010, A&A, 522, 36
- Kormendy, J., & Richstone, D. 1995, A&A, 33, 581
- Merritt, D., Ferrarese, L., & Joseph, C. L. 2001, Science, 293, 1116
- Nuñez, F. P., et al. 2012, A&A, 545, 84
- Onken, C. A., Ferrarese, L., Merritt, D., Peterson, B. M., Pogge, R. W., Vestergaard, M., & Wandel, A. 2004, ApJ, 615, 645
- Pancoast, A., Brewer, B. J., Treu, T., Park, D., Barth, A. J., Bentz, M. C., & Woo, J.-H. 2014, MNRAS, 445, 3073
- Papoulis, A. 1962, The Fourier Integral and Its Applications (New York: McGraw-Hill)
- Park, D., et al. 2012, ApJ, 747, 30
- Peterson, B. M., & Horne, K. 2004, arXiv:astro-ph/0407538
- Rosa, G. D., et al. 2015, arXiv:1501.05954v2
- Sergeev, S. G., Doroshenko, V. T., Dzyuba, S. A., Peterson, B. M., Pogge, R. W., & Pronik, V. I. 2007, ApJ, 668, 708

Shapovalova, A. I., et al. 2009, *NewAR*, 53, 191

Shields, G. A. 1999, *PASP*, 111, 661

Tremaine, S., et al. 2002, *ApJ*, 574, 740

Urry, C. M., & Padovani, P. 1995, *ASP*, 107, 803

Watson, D., Denney, K. D., Vestergaard, M., & Davis, T. M. 2011, *ApJ*, 740, 49

Woo, J.-H., et al. 2010, *ApJ*, 716, 269

Zu, Y., Kochanek, C. S., Kozłowski, S., & Peterson, B. M. 2013a, [arXiv:astro-ph/1310.6774](https://arxiv.org/abs/1310.6774)

Zu, Y., Kochanek, C. S., Kozłowski, S., & Udalski, A. 2013b, *ApJ*, 765, 106

Zu, Y., Kochanek, C. S., & Peterson, B. M. 2011, *ApJ*, 735, 80